THESIS FOR THE DEGREE OF LICENTIATE OF ENGINEERING

Corrosion of painted galvanized steel pretreated with Zr-based thin films

Konrad Tarka

Department of Chemistry and Chemical Engineering

CHALMERS UNIVERSITY OF TECHNOLOGY

Gothenburg, Sweden 2015

Corrosion of painted galvanized steel pretreated with Zr-based thin films
Konrad Tarka

Licuppsatser vid Institutionen för kemi och kemiteknik. 2015:15

ISSN : 1652-943X

Department of Chemistry and Chemical Engineering
Chalmers University of Technology
SE-412 96 Gothenburg
Sweden
Telephone + 46 (0)31-772 1000

Printed by Chalmers Reproservice
Gothenburg, Sweden, 2015

Cover:
Schematic illustration of corrosion blister at wet and dry sections of corrosion test cycle.

Corrosion of painted galvanized steel pretreated with Zr-based thin films

Konrad Tarka

Department of Chemistry and Chemical Engineering

CHALMERS UNIVERSITY OF TECHNOLOGY

Abstract

For decades, phosphating has been considered state of the art for pretreating car bodies in order to promote corrosion resistance and paint adhesion. Although it offers excellent corrosion protection, the phosphating process has drawbacks. These drawbacks include limits on how much aluminium can be used in a car body, high process costs due to heating the process baths, and high costs for wastewater treatment. The phosphating process also utilizes toxic metals, such as nickel, which are on the REACH list. Since the early 2000's, commercial alternatives to phosphate pretreatment have been available. These technologies are based on zirconium chemistry and have addressed the drawbacks with the phosphating process. There is limited knowledge regarding the paint delamination and corrosion behavior of automotive materials pretreated with these replacement technologies. In this work, the behavior of these zirconia-based technologies has been studied and compared to traditional phosphating. Utilizing an accelerated corrosion exposure regime, both short and long term exposures in atmospheric conditions have been used. Hot dipped galvanized (HDG) steel was used as a substrate. The resulting corrosion products have been analyzed using X-ray diffraction (XRD), scanning electron microscopy (SEM), and energy dispersive spectroscopy (EDS). It was found that the paint delamination mechanism did not differ between the different pretreatment technologies when using the current exposure method. The main corrosion product found was simonkolleite ($Zn_5Cl_2(OH)_8 \cdot H_2O$). It was also found that the scribe was the area of cathodic activity and that the zinc was dissolved anodically.

Keywords: HDG, cyclic corrosion test, SEM, XRD, EDS, Atmospheric corrosion

List of publications

The thesis is based on the following papers:

Paper I
K. Tarka, A. Jaako, D. Persson, H. Mattsson, L-G. Johansson
Corrosion propagation under paint films on galvanized steel - A comparison of phosphating and thin film corrosion pretreatment technologies
Proceedings paper, *Sustainable Automotive Technologies 2014, Proceedings of the 6th ICSAT*

Paper II
K. Tarka, A. Jaako, D. Persson, H. Mattsson, L-G. Johansson
Corrosion behaviour of zirconia based thin film pretreatments vs phosphating during short and long term cyclic exposure
Submitted to *Progress in organic coatings*

Statement of the author's contribution for Paper I
I was responsible for all of the sample preparation, excluding the application of pretreatment and paint systems. I conducted the majority of the analytical work and was present for the FT-IR microscopy measurements. All of the data analysis was carried out by me. The writing was mainly perfomed by myself and my supervisor Lars-Gunnar Johansson

Statement of the author's contribution for Paper II
I was responsible for all of the sample preparation, excluding the application of pretreatment and paint systems. I conducted the majority of the analytical work and was present for the FT-IR microscopy measurements. All of the data analysis was carried out by me. The writing was mainly performed by myself and my supervisor Lars-Gunnar Johansson The finalization of the paper before submission was performed by myself.

1. Background

Environmental legislations are forcing car manufacturers to develop vehicles which are more energy efficient. In order to decrease fuel consumption and CO_2 emissions, the automotive industry is striving to reduce body weight by using lightweight materials, i.e. aluminium. However, today's commercial pretreatment process (zinc phosphating) has difficulty handling increased amounts of aluminium due to poisoning and increased quantities of sludge in the bath. Moreover, there are environmental issues with the existing zinc phosphating processes. These issues involve the sludge that is created, as well as the health-issues associated with heavy metals, especially nickel, in the process. Additionally, energy and water consumption are high for the zinc phosphating processes.

In recent years, alternatives to phosphate have emerged on the market. One of the most promising technologies relies on mixtures of mainly zirconiumhexafluorides and silicone compounds. Some of the ingredients in the pretreatment mixtures are proprietary. In addition to containing fewer heavy metals, these technologies consume less water and energy. The new technologies also provide the possibility to pretreat aluminium and magnesium.

Knowledge about how these technologies work in the automotive pretreatment process, as well as how these technologies behave under a car's paint layers is scarce. What is known about the new pretreatment technologies is that they theoretically have an ability to offer good corrosion protection and good paint adhesion. Also, in laboratory testing, the Next Generation Pretreatments (NGP) give approved corrosion results. Though, they do not reach the performance level of zinc phosphating for steel. What is relatively unknown is how NGP´s perform on a car after a few years in operation. Some results seem to indicate that corrosion problems, which are not captured in lab testing, may occur in the field.

The lesson learnt from history is that there is a paramount risk with new pretreatments. In the mid-1970's, the introduction of new car body pretreatments and paint procedures resulted in almost catastrophic problems with corrosion. These problems affected most car manufacturers.

The scope of this thesis is to compare and contrast the corrosion behavior of thin film treated and phosphate painted galvanized steel for automotive applications. The samples were exposed to cyclic corrosion conditions in a laboratory environment. The results are compared with regards to morphology of the resulting blisters, as well as corrosion products.

2. Theory

Iron and zinc rank first and fourth among metals produced globally [1]. Steel is the main construction material used by the automotive industry [2]. Since the late 1970's, the use of zinc coated steel cars has increased. Today, zinc coating is the dominant application for car bodies [3]. Zinc coating on steel supplies cathodic protection due to the lower corrosion potential of zinc [4].

2.1 Corrosion

Corrosion of metals and alloys in aqueous solution is usually an electrochemical process [4]. The corrosion cell contains an anode and a cathode, which are connected electronically, as well as by an ionically conducting medium (an aqueous electrolyte). This is exemplified in equations 2.1 and 2.2 for zinc metal in a solution.

$Zn(s) \rightarrow Zn^{2+}(aq) + 2e^-$ Anodic reaction (2.1)

$1/2\ O_2(aq) + H_2O(l) + 2e^- \rightarrow 2OH^-(aq)$ Cathodic reaction (2.2)

The cell reaction becomes:

$Zn(s) + 1/2\ O_2(aq) + H_2O(l) \rightarrow Zn^{2+}(aq) + 2OH^-$ (2.3)

The oxygen reduction reaction (2.2) has been shown to be the case for clean metal surfaces. On oxidized surfaces, stable intermediate products, such as superoxide ion radicals (O_2^-) and peroxyl ions (HO_2^-), have been reported by Wroblowa et al [5].

For a cell reaction to be thermodynamically allowed, the change in Gibbs free energy ΔG must be <0.

Because

ΔG = -nFE (2.4)

where *n* is the number of electrons, *F* is Faraday's constant, and *E* is the cell potential in volts. This implies that, for a reaction to be spontaneous the cell potential, *E* has to be positive.

From equation 2.4 the Nernst equation can be derived. For a general half-cell reaction $M^{n+} + ne^- \leftrightharpoons M$, Nernst's equation at 25°C can be written as

$e = e^\circ + \left(\frac{0.059}{n}\right) \log[M^{n+}]$ (2.5)

Here *e* is the equilibrium potential and *e*° is the standard half-cell potential. If the sum of the cathodic half-cell potential, e_c, and anodic half-cell potential, e_a, is positive, the reaction will proceed spontaneously to the right. If the potential is negative, the reaction will proceed spontaneously to the left. By using the Nernst equation, it is possible to construct potential/ pH diagrams, so called Pourbaix diagrams. These diagrams demonstrate the spontaneous direction of the reactions under given conditions. Pourbaix diagrams for zinc are shown in Figure 3.1 together with predominance diagrams for the Zn-Cl and Zn-pH systems [6]–[8].

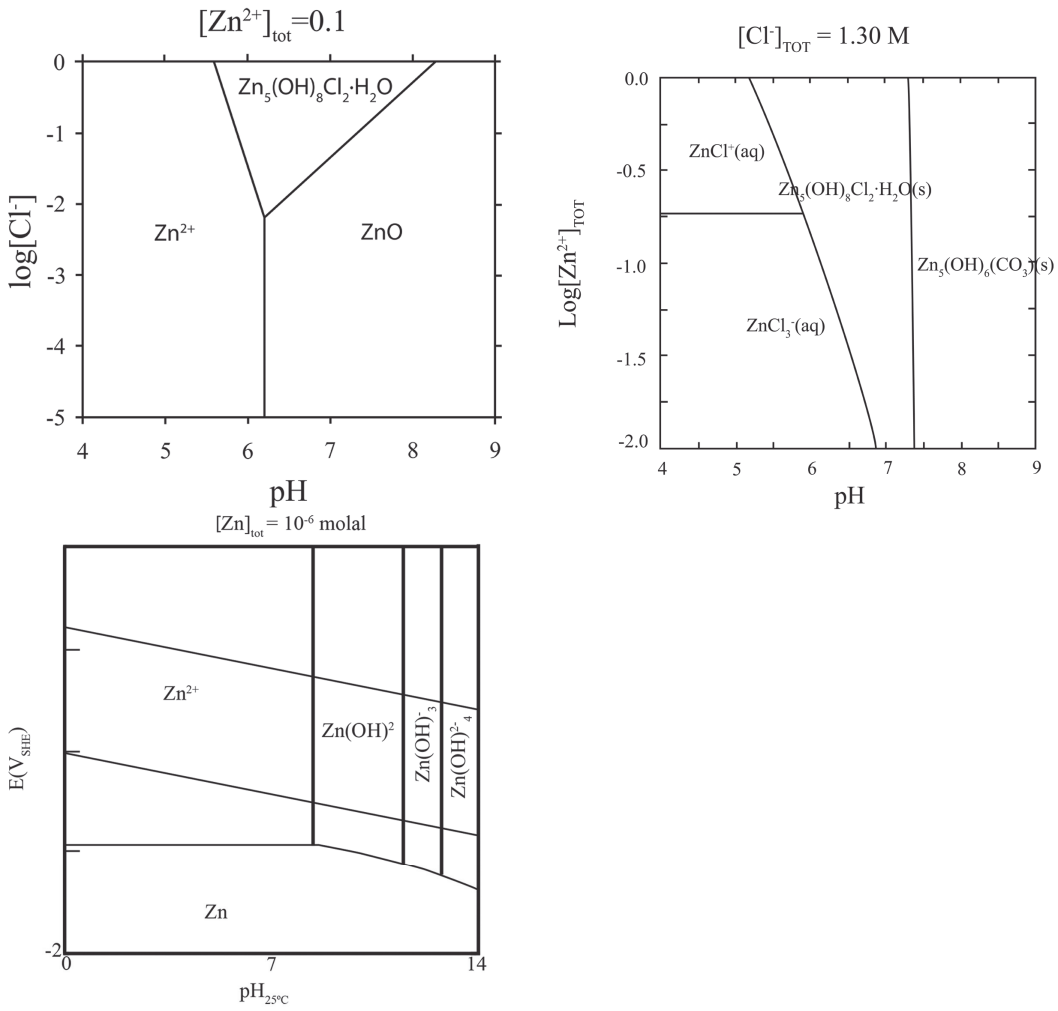

Figure 2.1 In the top row, the predominance diagrams for the Zn-Cl and Zn-pH systems are shown [7], [8]. The Zn Pourbaix diagram is shown at the bottom [6].

2.2 Atmospheric corrosion

Atmospheric corrosion is the corrosive degradation of materials when exposed to atmospheric conditions. It is usually an electrochemical process with anodic and cathodic reactions, as described above. The atmosphere primarily consists of N_2 (78,08%) and O_2 (20,95%), as well as CO_2 (390,5 ppb). There are also traces of the noble gases He, Ar, Kr, Ne, and Xe. [9], [10]. O_2, CO_2 and H_2O play major roles in the atmospheric corrosion of Zn. Other minor compounds found in the atmosphere, and which may influence corrosion, are O_3, H_2O_2, SO_2 , H_2S, COS, NO_2, HNO_3, NH_3, HCl, Cl_2 , HCHO, and HCOOH, whose total amount in the atmosphere is below 10 ppb. Depending on temperature and relative humidity, the water vapor concentration in the atmosphere varies between 100 ppm and 10000 ppm [10].

Due to the variations in concentration of pollutants, the atmosphere can be classified into different types: rural, industrial and urban [11]. In table 2.1, the different classifications are presented together with the concentrations of pollutants.

Table 2.1 Pollutants in the atmosphere. All pollutant concentrations are given in ($\mu g*m^{-3}$) except for "Particles (Dust deposits)" and "Soot" which are given in ($mg*m^{-2}*y^{-1}$) [11]

		SO_2	NO_2	HNO_3	O_3	H_2S	Cl_2	Particles - PM10	Particles (Dust deposits)	Soot
Area	Rural	2-15	2-25	0,1-0,7	20-90	N/A	N/A	10-25	450-1500	<5
	Industrial	50-400	N/A	0,5-4	20-90	N/A	N/A	30-70	1000-6000	≤75
	Urban	5-100	20-150	0,5-4	20-90	20-250	≤20	30-70	1000-6000	≤75

Water molecules adhere to metals and oxides exposed to the atmosphere. The number of molecule layers depends on the relative humidity in the environment [10]. In atmospheric corrosion, it is more relevant to consider liquid water. Water can be deposited by condensation, fog, rain, splashing, as well as by deliberately cleaning and rinsing a surface using water. Pure water will not result in significant corrosion due to the low concentrations of ions [4], [12]. In order for significant corrosion to occur, pollutants need to be introduced to the water layer. This can be done by either wet deposition or dry deposition. Wet deposition occurs when pollutants are dissolved in the water deposits. Dry deposition occurs when the pollutants deposit as gas molecules or other pollutants. Dry deposition occurs most often in indoor environments, whereas wet deposition occurs in the outdoor environment. The effects of pollutants on the corrosion of zinc have been studied by a number of authors [7], [8], [13]–[16]. Selected results from Svensson's thesis are summarized in figure 2.2, which shows the corrosion rates at 95 %RH following four weeks of exposure. The figure shows that the addition of SO_2 in the atmosphere increases the corrosion rate of pure zinc when compared to pure air, NO_2 and O_3. There are also synergetic effects reported when mixing the pollutants, as seen in figure 2.2 [17].

The outdoor atmospheric conditions vary periodically with regards to temperature and humidity [18]. This causes the material surface to alternate between wet and dry [19]. The dehydration of electrolytes saturates the electrolyte with pollutants and facilitates the precipitation of corrosion products. These corrosion products can passivate the metallic surface.

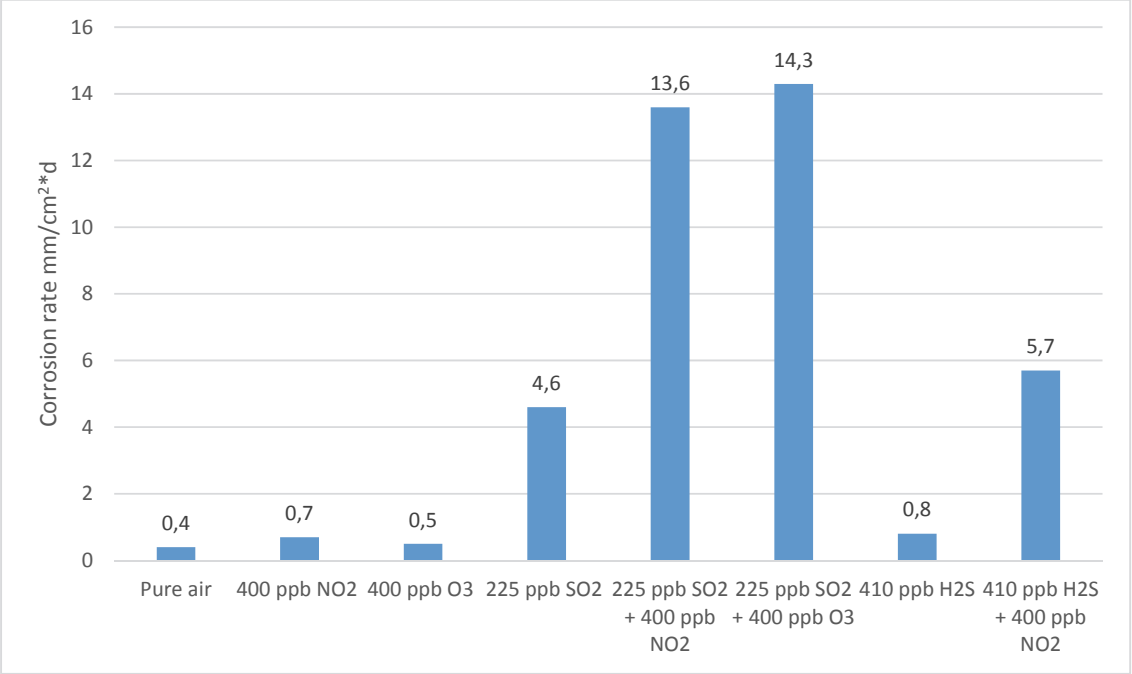

Figure 2.2 The corrosion rates of zinc when exposed to different pollutants [17].

2.3 The influence of NaCl on the corrosion of zinc

The most important corrosion accelerator in automotive corrosion is NaCl, which is used in deicing and dust binding applications on road surfaces. The effect of NaCl on the corrosion of zinc has been described in a number of works, for instance Svensson's thesis [17] and by Lindström et al [8]. The deliquescence point for NaCl is 75% RH, meaning that for humidity ≥ 75% RH deposited salt crystals will form a solution establishing electrochemical corrosion cells. The aqueous ions are transported by the potential field that arises between the anode and cathode. The anions are transported towards the anode and the cations are transported towards the cathode. Thus, the anode is enriched in chloride and cathode in sodium. The corrosion products found on zinc in NaCl containing environments are simonkolleite, $Zn_5Cl_2(OH)_8 \cdot H_2O$), but also ZnO [7], [20], [21]. Environments containing other pollutants are known to produce different corrosion products on zinc. A selection is presented in Table 2.2. There is a positive temperature dependency for the corrosion rate of zinc in NaCl containing environments. This corrosion rate was reported to increase 10 times in the temperature range between 4 and 38°C [7]. When zinc is subjected to cyclic corrosion conditions in a NaCl containing environment, the corrosion product composition changes as the cycles are altered. Zhu et al showed that as the dry periods got longer the corrosion products on open zinc surfaces were dominated by simonkolleite [22].

Table 2.2 Corrosion products formed on zinc metal in different environments.

Corrosion products detected	Environment	RH (%)	Reference
$Zn_5Cl_2(OH)_8 \cdot H_2O$	NaCl, NaCl + SO_2, NaCl + NO_2, NaCl + SO_2 + NO_2, NaCl +CO_2	70 and 95	[7], [8], [21]
$Zn_3CO_3(OH)_6 \cdot H_2O$	NaCl + CO_2	95	[7], [8]
$Zn_5(NO_3)_2(OH)_6 \cdot 2H_2O$	HNO_3	65	[15]
$ZnSO_4 \cdot 3Zn(OH)_2 \cdot 4H_2O$	NaCl + SO_2	70	[21]
ZnO	NaCl, NaCl + SO_2, NaCl + NO_2, NaCl + SO_2 + NO_2	70	[21]
$ZnSO_4 \cdot 3Zn(OH)_2NaCl \cdot 6H_2O$	NaCl + SO_2, NaCl + SO_2 + NO_2	70	[21]

2.4 Zinc coated steel

Coating steel with Zn provides the steel with galvanic protection whereby the Zn dissolves preferentially due to the higher nobility of iron compared with zinc. There are several processes for applying a zinc coating to steel, such as hot dip galvanizing (HDG), electroplating, spraying, and painting. This thesis focuses on HDG material. HDG steel is produced by dipping the steel in molten zinc. Aluminium is used as an alloying element to promote the formation of a $Fe_2Al_{5-X}Zn_X$ layer at the Zn – steel interface, thereby preventing the diffusion of Fe into the zinc layer. Alloying with aluminium also results in formation of aluminium oxide at the surface of the coating, as well as aluminium enrichment in the grain boundaries. The zinc grains are preferentially oriented with the basal plane (0002) normal to the surface[23]. In order to promote the retention of lubricants and corrosion inhibitors, the zinc coated sheet is often imprinted using rollers with a specific texture, such as an electron discharge texture (EDT) or an electron beam texture (EBT)[24], [25]. The mechanical deformation of the zinc layer causes it to partly recrystallize, which results in smaller sized grains in the depressed areas when compared to the plateau areas [23]. A typical thickness of the zinc coating for automotive exterior panels is 7,5 μm [26].

2.5 Corrosion protection of automotive sheet metal

The paint systems used to coat the car body are comprised of several layers. In this section, the different layers and their functions will be described for automotive outer panels. The outer panel on a conventional automotive structure consists of galvanized steel sheet, see section above. The different layers are schematically shown in Figure 2.3.

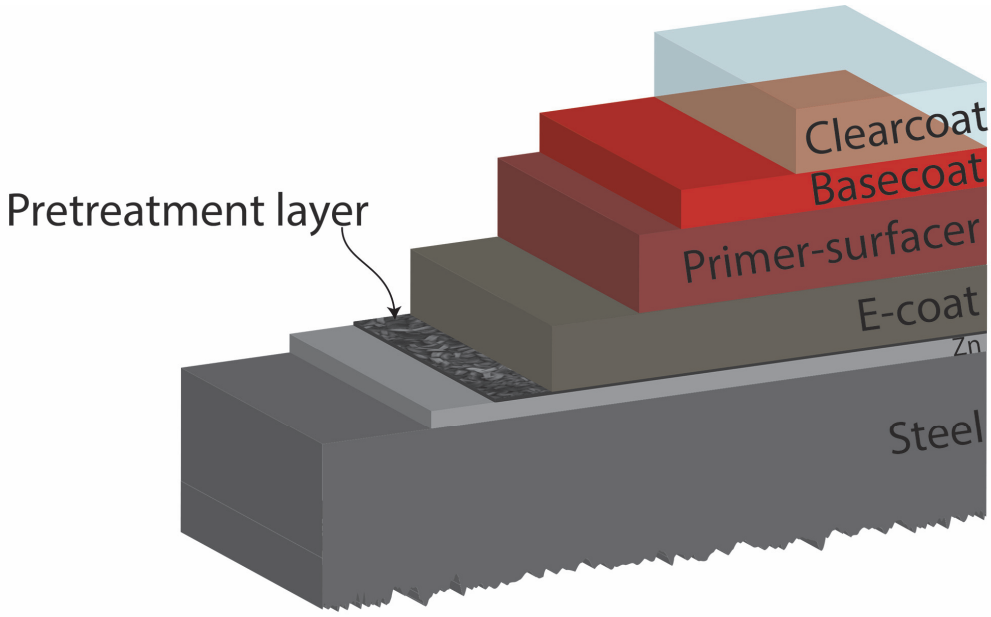

Figure 2.3 Schematic view of the layers composing a traditional automotive paint system.

The first layer applied on the car body is a conversion coating. This layer is designed to provide corrosion protection, as well as to promote adhesion of the subsequent paint layers. The conversion coating most widely used is phosphating. On top of the conversion coating, an electrophoretic paint is applied by a dipping process. This electrophoretic paint provides additional corrosion protection. The following paint layers are applied by spraying. The primer surfacer adds mechanical toughness and stone chip resistance. Subsequently, a basecoat containing pigment is applied. In certain cases, metallic and/or mica flakes are added for decorative effect. The final coating is a clearcoat designed to resist scratches and give UV protection to the coatings below [27].

2.5.1 Phosphating

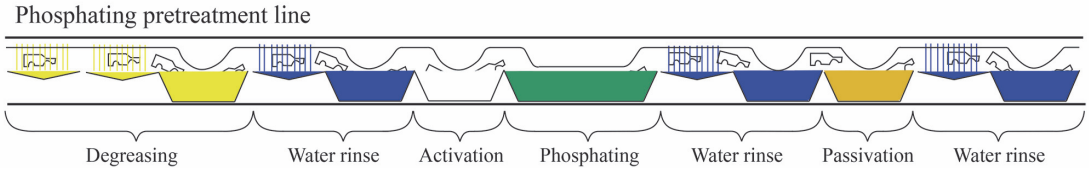

Figure 2.4 Schematic view of an automotive dip phosphating line.

Phosphating is applied in a continuous process consisting of seven steps. In Figure 2.4, a dip line process is shown. The process steps are: degreasing, rinse, activation, phosphating, rinse, passivation, and final rinse [28].

2.5.2 The phosphating step

The main step in the phosphating process is carried out in a phosphating bath where the coating is precipitated onto the car body. After nearly one hundred years, the use of phosphated steel is widespread in the automotive industry [28]. The phosphated surface is morphologically characterized by micrometer sized crystals and is applied by either a spray

or a dip process [28], [29]. The phosphating solution contains dilute phosphoric acid combined with different additives which are intended to control the morphology of the coating, as well as the surface coverage. The phosphate solution is tailored according to the material mix of the car body to be phosphated [30].

The general deposition of the phosphate layer on galvanized steel is described below. The substrate is dissolved at low pH in the phosphate bath. At micro cathodic sites, hydrogen is evolved. This increases pH and causes phosphate to precipitate. In the case of zinc the phosphate formed is $Zn_3(PO_4)_2 \cdot 4H_2O$ (hopeite). The reaction is summarized in equation 3.6 [28], [31].

$$3Zn^{2+}(aq) + 4H_2O(l) + 2H_2PO_4^-(aq) \rightarrow Zn_3(PO_4)_2 \cdot 4H_2O(s) + 4H^+(aq) \quad (3.6)$$

The size of the crystals is in the range of a few micrometres up to 100 µm. In modern automotive applications, a tri-cationic phosphate containing Zn, Ni and Mn ions is used. These form a doped hopeite $Zn_{3-x}Me_x(PO_4)_2 \cdot 4H_2O$ where Me is Ni and/or Mn. The addition of Ni^{2+} and Mn^{2+} increases the crystal growth rate and the corrosion resistance. [28].

The surface coverage of the phosphate coating is in the range of 98,5-99,5% [32]. The adhesion mechanism between the phosphate layers and the subsequent paint layers is of a "lock and key" fashion. This, in combination with the barrier properties of the coating, is the main contribution of phosphate to the corrosion resistance [33].

2.5.3 The activation step

In order to achieve a uniform phosphate coating, an activation of the metal surface is performed in process step 3 (Figure 2.4). Activation is achieved by colloidal titanium phosphate, which acts as nucleation sites for the phosphate crystals. The enhanced nucleation gives a higher surface coverage and smaller crystal size [34].

2.5.3.1 Degreasing

As the car body leaves the stamping and assembly plants, oil, grease, particles and oxides are present on the surface. As such, cleaning the surface is essential for phosphating. Degreasing is the first step in the phosphating process (see Figure 2.4). Cleaners for automotive applications are often composed of an organic and an inorganic component and used at an alkaline pH. The organic component is often a non-ionic surfactant and the inorganic compound can be borate or silicate. The high pH causes hydrolyzation of oils present on the surface. The surfactants remove any mineral oil which was not hydrolysed by the high pH. The borates and silicates act as a corrosion inhibitors, bath stabilizers and pH buffers [35]. High agitation and good penetration in hidden areas of the car body are needed in order for degreasing reach its maximum potential. For this reason, the degreasing step is often a combination of high pressure spray and dip treatments as seen in Figure 2.4 [28], [36].

2.5.3.2 Rinsing

After the major steps in the phosphating process, rinsing is essential. Rinsing interrupts ongoing reactions on the surface and prevents the transference of chemicals from one bath to the next; thus, avoiding contaminating the baths downstream in the process [30].

2.5.4 Paint system

2.5.4.1 Electrophoretic coating

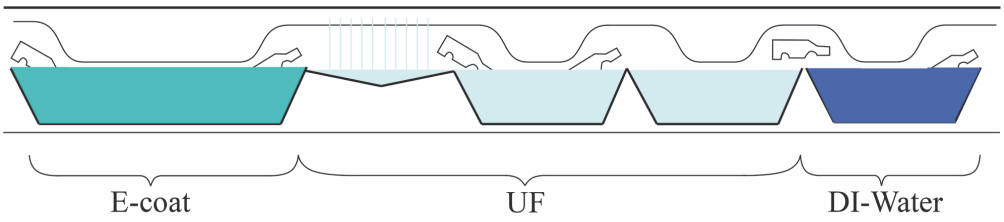

Figure 2.5 Schematic of E-coat application line

The electrophoretic coating (E-coat), which provides additional corrosion resistance, is the first paint coat applied after pretreatment. E-coatings have been used in the automotive industry since the 1960's. This process is performed in a dipping line (Figure 2.5) by using an E-coat with charged paint particles. The car body is biased towards the E-coat bath, allowing the paint to adhere to the car body, as well as to allow the paint to penetrate into crevices (the ability to penetrate into crevices is generally called throwing power). The first E-coats used were anodic. Due to better corrosion performance, the E-coat has been changed to a cathodic type, which is still state of the art in the automotive industry.

The E-coat bath is an aqueous solution with three main components:

- charged pigment droplets with special solubilized resin
- an aqueous polymer solubilized with acid
- coalescing solvents

After E-coating, the body is transported to an oven where the coating is allowed to crosslink at 180°. The thickness of the E-coat is usually 25µm [26]. The E-coat is sensitive to UV radiation and needs to be protected by additional coatings in exposed areas.

2.5.4.2 Primer surfacer, basecoat and clear coat

Typically, three additional coatings are applied after E-coating. In order, these are: primer surfacer, basecoat and clearcoat. Each coating has its own specific function; although, they all act together to create a barrier in order to prevent water or ions reaching the metal surface. The three coatings are applied by manual spraying or by robotic spray application. The current trend within the automotive industry is to decrease the number of coatings for economic reasons [27].

Primer surfacer

The primer surfacer hides any imperfections that are still present after E-coating. The thickness of this coating is in the range of 30-40 μm. The primer surfacer also increases the overall stone chip resistance of the paint system. A primer surfacer is important as it helps to prevent stone and other debris, which are propelled against the vehicle during operation, from damaging the coating down to the metallic substrate. Such damages can lead to corrosion [26].

Basecoat

The basecoat contains the pigment that gives the car body its color. It is in this layer that additions of aluminium or mica flakes can be made to give the paint a metallic or pearlescent finish. Other functionalities include UV barrier properties to protect the E-coat and surfacer from UV radiation. The layer thickness of the basecoat is usually 15-25 μm. Due to stricter emission regulations regarding volatile compounds, solvent based basecoats are being replaced by water based ones [26], [27].

Clearcoat

A clear coat is applied to give the final appearance. It serves to protect against scratches, as well as to provide a barrier against UV radiation and chemical degradation of the underlying layers. The thickness of the clearcoat is usually between 35-50 μm [26], [27].

2.5.5 Thin film pretreatments

The relatively high cost of the phosphating process has sparked an interest in finding suitable replacement. The high cost for the phosphating process is due in part to high energy consumption, as well as to the complex wastewater treatment required due to usage of heavy elements such as Ni and Mn.

2.5.5.1 Zr and Ti based pretreatments

The Zr and/or Ti based pretreatments result in the formation of a thin conversion coating consisting of Zr or Ti oxide, or a Zr/Ti mixed oxide. These types of coatings have been studied by Adhikari et al, by Lunder et al, by Nordlien et al and by George et al [37]–[41]. Nordlien, George and Lunder used aluminum AA6066 substrates, and Adhakiri used cold rolled steel as substrates. The conversion coating can be applied in a dip or spray process by applying a H_2ZrF_6 and/or H_2TiF_6 containing solution. Similar to the phosphate coating, the Zr/Ti based process relies on cathodic nucleation to deposit on the substrate [42]. The deposition mechanism on aluminum is described below [40]. The deposition mechanism on CRS (Cold Rolled Steel) and HDG substrates is believed to be similar to the deposition on aluminium.

Dissociation of the acid (equation 2.6).

$$H_2ZrF_6 \Rightarrow 2H^+ + ZrF_6^{2-} \quad (aq) \tag{2.6}$$

The acid promotes the dissolution of the metal, in this case aluminium (equation 2.7)

$$Al(s) \Rightarrow Al^{3+}(aq) + 3e^- \tag{2.7}$$

The aluminium forms fluoride complexes releasing Zr^{4+} ions into the solution (equation 2.8)

$$Al^{3+}(aq) + ZrF_6^{2-}(aq) \Rightarrow Zr^{4+}(aq) + AlF_6^{3-}(\text{aq}) \tag{2.8}$$

At local cathodic sites on the aluminium surface, consisting of noble inclusions in the material or impurities, hydrogen evolution occurs (equation 2.9)

$$2H^+(\text{aq}) + 2e^- \Rightarrow H_2(\text{g}) \tag{2.9}$$

The resulting increase in pH causes precipitation of hydrated Zr oxide (equation 2.10) occurs first on the nucleation sites; and then, forms a film over the surface. The resulting ZrO_2 layer has varying thickness and can be described as consisting of Zr oxide islands in a thin Zr oxide film.

$$Zr^{4+}(aq) + 3H_2O(l) \Rightarrow ZrO_2 \bullet H_2O(s) + 4H^+(aq) \tag{2.10}$$

The thickness and uniformity of the pretreatment layer depends on the distribution of intermetallic phases in the alloy [40].

To increase the density of cathodic sites the addition of Cu and Fe ions to the H_2ZrF_6 bath have been studied by Lostak et al and Adhikari et al [37], [43]. The addition of Cu ions increases the amount of deposited $ZrO_2 \bullet H_2O$ on both Zn and Fe substrates [37]. During pretreatment of HDG, deposition of metallic Cu and Fe is believed to occur during the dissolution of Zn according to equation 2.11 and 2.12 [43].

$$3Zn(s) + 2Fe^{3+}(aq) \rightarrow 3Zn^{2+}(aq) + 2Fe(s) \tag{2.11}$$

$$Zn(s) + Cu^{2+}(aq) \rightarrow Zn^{2+}(aq) + Cu(s) \tag{2.12}$$

The pretreatment layers are sensitive to surface contamination, i.e. inadequate cleaning. Other sensitive factors for the coating deposition are bath parameters, where excessive concentration of fluoride, iron and aluminium can result in irregular coating deposition [44].

2.5.5.2 Silane based films

The group of monomeric organosilicon molecules discussed below will be referred to as silanes, as this is the term used in the relevant literature. Silane films are formed from silane monomers in a solution. These monomers are of two basic types; mono-silanes and bis-silanes, where the first have one functional group attached and the latter has two functional groups attached. The basic structure for the silane monomers are presented below (2.13-2.15). The silane monomers undergo hydrolysis according to the equation 2.16. The hydrolyzation enables the silanes to attach to the hydroxylized oxide film present on the metallic substrate by condensation (2.18). Condensation (2.17) also promotes the gelation and precipitation of the silane film. Both the condensation and hydrolysis reaction rates are pH dependent. Thus, high rates of condensation and gelation occur when the concentration of OH^- is high. The hydrolyzation is dominant at low pH [45]. It has been shown that the condensation and hydrolysis reactions have a rate minimum at pH 7 and pH 4,3 respectively. This is valid for gamma-aminopropyltriethoxysilane (APS), gamma-3-methacryloxypropyl-trimethoxysilane (MPS), gamma-glycidoxypropyltrimethoxysilane (GPS) and gamma-ureidopropyltrimethoxysilane (UPS) [46]. It has been shown that to minimize condensation and subsequent gelation of silanes the silane concentration should be below 1 wt% [47]. Arkles et al have also shown that long carbon chains of the alkoxy group contribute to a slower condensation rate.

$$(R-O)_3Si(CH_2)_nY \tag{2.13}$$

$$(R-O)_3Si(CH_2)_nY(CH_2)_nSi(O-R)_3 \tag{2.14}$$

$$(R-O)_3Si(CH_2)_mSi(O-R)_3 \tag{2.15}$$

Where

$$R = methyl\ (-CH_3) or\ ethyl\ (-C_2H_5)$$

$$Y = -C_3H_6NH_3, -NH\ or\ -S_4$$

The silane films can consist of a single silane or a mixture of several silane compounds. The most commonly used silanes are listed below ([45]).

Table 2.3 Summary of most commonly used silanes, their chemical formula and classification

Name	Structure	Type
Vinyltriacetoxy silane	CH_2=CH-Si(OCOCH$_3$)$_3$	Mono-silane
Bis-1,2-(triethoxysilyl) ethane	$(C_2H_5O)_3Si$-CH_2CH_2-$Si(OC_2H_5)_3$	Bis-silane
Bis-[trimehoxysilylpropyl]amine	$(CH_3O)_3Si$-$(CH_2)_3$-NH-$(CH_2)_3$-$Si(OCH_3)_3$	Bis-silane
Bis-[trimethoxysilylpropyl]tetrasulfide	$(CH_3O)_3Si$-$(CH_2)_3$-S_4-$(CH_2)_3$-$Si(OCH_3)_3$	Bis-silane

$$(R-O)_3Si(CH_2)_nSi(O-R)_3 + 6H_2O \leftrightharpoons (HO)_3Si(CH_2)_nSi(OH)_3 + 6R-OH \quad (2.16)$$

$$-Si-OH + HO-Si \leftrightharpoons -Si-O-Si- + H_2O \quad (2.17)$$

$$-Si-OH + HO-Me \leftrightharpoons -Si-O-Me + H_2O \quad (2.18)$$

The partially polymerized silanes adhere to the metallic substrate by hydrogen bonds and form a viscous gel on the substrate surface. When the film is dried, the silanol and metal hydroxide groups condense to form metalo-siloxane bonds (equation 2.18) shown in Figure 2.6 [48]. Further condensation occurs in the film, which results in a crosslinked network. The temperature to obtain maximum curing ranges from room temperature to 100°C [45]. After curing, the film thickness is in the range of 50 nm – 500 nm. Thick films have some unfavorable characteristics, such as brittleness and cracking.

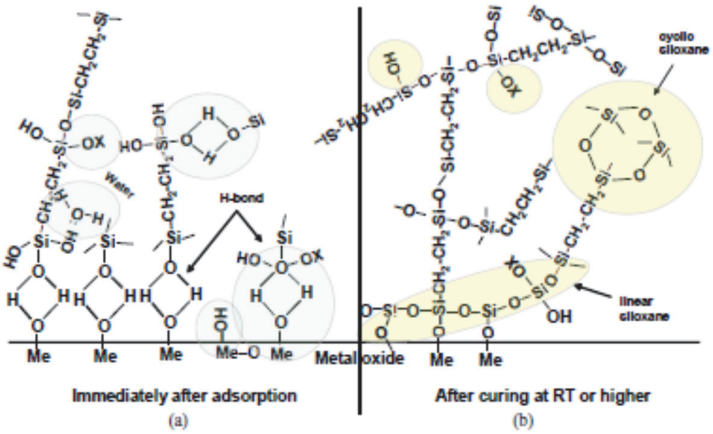

Figure 2.6 Deposition and formation of silane network in a metal surface [48].

Impedance measurements suggest that the resulting films consist of several layers. Thus, it has been suggested that close to the metal-silane interface there is a layer containing $Si-O-Me$ and $Si-O-Si$ bonds with a thickness of about 5 nm. Further out, the layer contains $Si-O-Si$ and unhydrolyzed $Si-OH$ bonds. The top layer contains bonds between the silane network and the paint layer [45], [49]. A schematic representation of the layer can be seen in Figure 2.7.

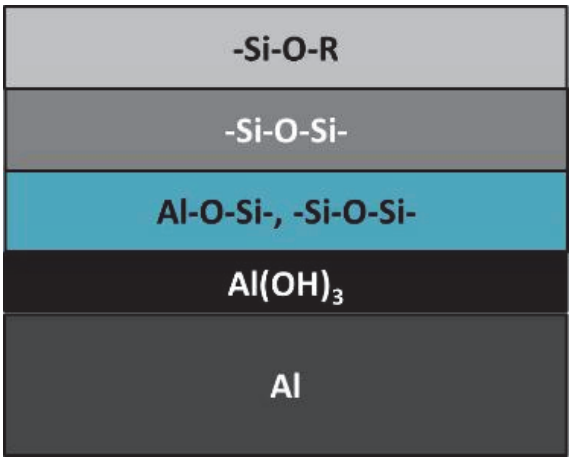

Figure 2.7 Schematic representation of the silane layers on aluminium substrate.

2.5.6 Commercial thin film pretreatment processes – mixed Zr- and Si technology films

Commercially available thin film coatings often combine the Zr/Ti technology and a silicone based technology in the same process. Studies have shown that after application, the resulting coatings have an increased concentration of Zr closest to the metallic surface and an increase in Si concentration furthest from the substrate [50]. The resulting coating thickness is between 20 and 100 nm [39] Although the phosphate conversion coating and the thin film conversion coatings differ in chemistry, the set up for the process is similar. However, the activation step needed for phosphating (see Fig. 2.4) is omitted and silicate containing cleaners cannot be used [36], [51].

2.6 Underpaint corrosion and delamination on phosphated HDG

Several delamination and corrosion mechanisms have been proposed for zinc phosphate (ZnPh) pretreated HDG steel which has been coated with a polymer coating during cyclic corrosion tests. The common morphology of the corrosion blisters that propagate from damage that penetrates both paint and zinc layers is shown in Fig. 2.8. Typically, a primary blister is formed; sometimes, secondary, tertiary or even higher order blisters also form. Blistering has been described in a review paper by Amirudin at al [52]. Three different modes of paint delamination have been distinguished for HDG steel:

1. Cathodic delamination
2. Anodic undermining
3. Anodic undermining and mechanical delamination

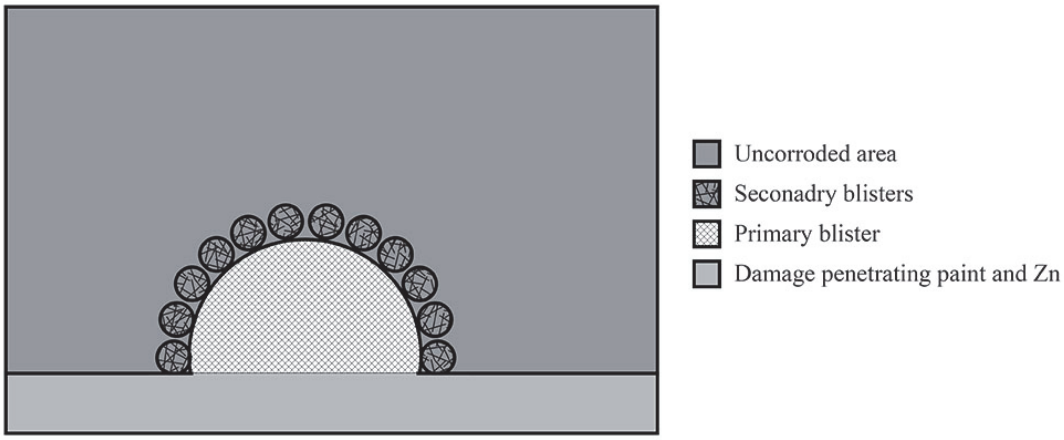

Figure 2.8 Schematic view of a primary blister surrounded by secondary blisters propagating from a damage in the paint.

2.6.1 Cathodic delamination

It has been proposed by several authors, including Fürbeth and Stratmann and Granata [53]–[58], that the delamination mechanism of painted galvanized steel is cathodic. The cathode is supposed to be at the corrosion front in the interface between zinc and the polymeric coating with and a trailing anode or an anode situated in a coating defect [52]. Oxygen transport to the cathode occurs through the polymeric coating or in the interface between paint and zinc [59]. It can be noted that the systems used to show these mechanisms were model samples using non pigmented polymeric coatings [60] without any pretreatment of the metal surfaces prior to application of the coating.

Several mechanisms for coating disbonding have been proposed. Degradation of the polymeric coating near the zinc/coating interface due to high pH is often shown. [52]. As is a degradation of the phosphate coating [61]. Granata proposed a mechanism with a mechanical component that can occur in using cyclic conditions [56]. The mechanism proposed consists of four parts and is shown in Figure 2.9:

1. Initial cathodic reduction of oxygen at the zinc/paint interface, increasing the pH and weakening paint-phosphate and phosphate-zinc bonds.
2. During the drying portion of the cycle, corrosion products precipitate and apply mechanical stresses on the paint film.
3. Mechanical delamination of the paint/zinc interface occurs allowing oxygen to access the newly exposed area.
4. Further oxygen reduction occurs and mechanical delamination of the paint advances the corrosion.

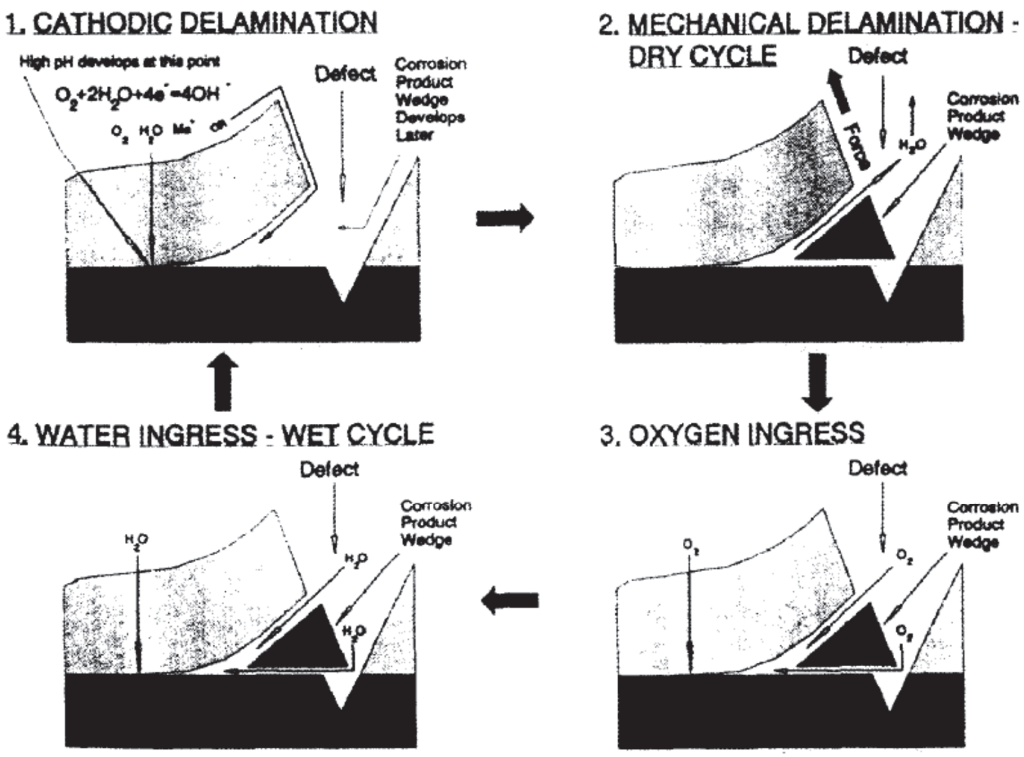

Figure 2.9 Illustrations of the mechanism proposed by Granata for cathodic coating delamination [56].

2.6.2 Anodic undermining

In anodic undermining, the cathodic area is located in damage in the paint, i.e. a scribe that cuts through the paint system and zinc coating, or at a cut edge. In this scenario, which has been suggested by a number of authors [62]–[67], oxygen reduction takes place on the exposed steel surface. The corresponding anodic reaction takes place in the zinc coating causing dissolution. Zinc dissolution takes place beneath the ZnPh pretreatment layer and is not directly affected by the pretreatment. Anodic undermining was demonstrated by Nazarov in a NaCl(aq) thin electrolyte by inducing a damage to the steel on a galvanized substrate.

2.6.3 Anodic undermining and mechanical delamination

This mechanism is similar to the anodic undermining described above. In this case, the osmotic pressure of the electrolyte helps to delaminate the paint. Thus, the anodic dissolution causes accumulation of $ZnCl_2$ (aq) under the paint film. By osmosis water diffuses into the blisters. The resulting volume increase causes delamination of the weakest interface ahead of the corrosion front supplying fresh anodic sites to the corrosion cell [52], [61].

3. Analysis methods

3.1 Scanning Electron Microscope (SEM)

The SEM uses electrons to observe and gain information from samples. The electrons are emitted from an electron gun, which can either be of a field emission or thermionic type. The thermionic type heats up a filament, which is often made of W or LaB_6, until it emits electrons. In a field emission gun the electrons are extracted by applying high voltage over a sharp tungsten tip. The electrons emitted from the electron gun are accelerated by a high voltage bias. In an SEM, the accelerating voltages typically range from <0,2 keV to 30 keV. The electrons travel through the microscope column and are focused onto the sample via magnetic lenses into a small probe. The probe is then scanned across the sample by scanning coils. In Figure 3.1, a schematic image of the construction of a SEM.

When the electron beam hits the sample the electrons will penetrate into the material. The depth of penetration will depend on the energy of the electrons, and the density of the material. The volume that is created by the penetrating electrons is referred to as interaction volume. This volume increases as the electron energy increases and as the density of the material decreases. A simulation of the interaction volume at different accelerating voltages and with different materials was performed using Casino v.2.48 software. The results of this simulation are shown in Fig. 3.2.

Several signals are emitted from the sample as the electron beam hits the material; they are summarized in Figure 3.3. The most commonly used signals are secondary electrons (SE), backscattered electrons (BSE) and characteristic X-rays. The secondary electrons are used to obtain topographic contrast. The electrons are detected with a secondary electron detector. This detector has a grid where a bias is applied to increase the collection of the electrons. The secondary electrons have a low energy, typically less than 50 eV. The low energy of the electrons permits only electrons generated close to the surface to escape the sample and be detectible. The backscattered electrons are used for Z-contrast. This means that the contrast seen in the images will depend on the mean atomic weight of the imaged region. Areas of the sample with a lower mean Z-number will appear darker than areas with higher mean Z-number. The backscattered electrons can have energies up to the energy of the incident beam. The high energy of the BSE electrons results in images with lower surface sensitivity and resolution as the electrons are emitted from a larger portion of the excitation volume [68].

The SEM imposes certain constraints on the investigated samples. The samples need to be conductive; otherwise the samples will charge up and degrade the image. The samples to be observed also need to withstand the vacuum conditions present in the chamber. To be able to observe nonconductive samples, such as certain corrosion products, one can coat the samples with a conductive coating, e.g. gold or carbon. One can also introduce a gas into the specimen chamber. The gas molecules will be ionized by the electron beam and create a path for the built up charge on the sample to dissipate. The increased pressure in the chamber will have adverse effects on the resolution of the image due to spreading of the beam.

Two different scanning electron microscopes were used in this work, a FEI Quanta200 FEG-ESEM and a Zeiss EVO Ma15 with a LaB_6 cathode.

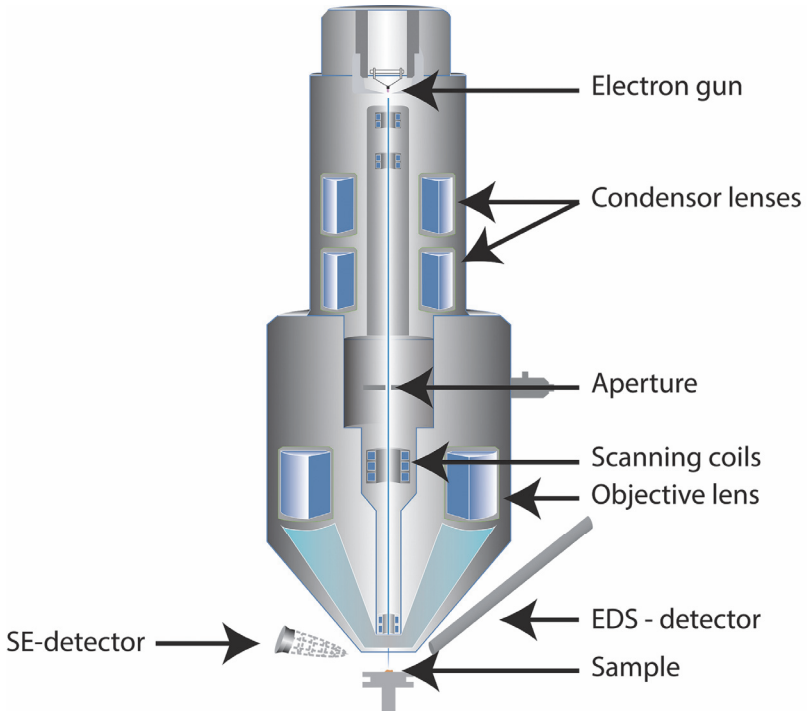

Figure 3.1 Schematics of a SEM

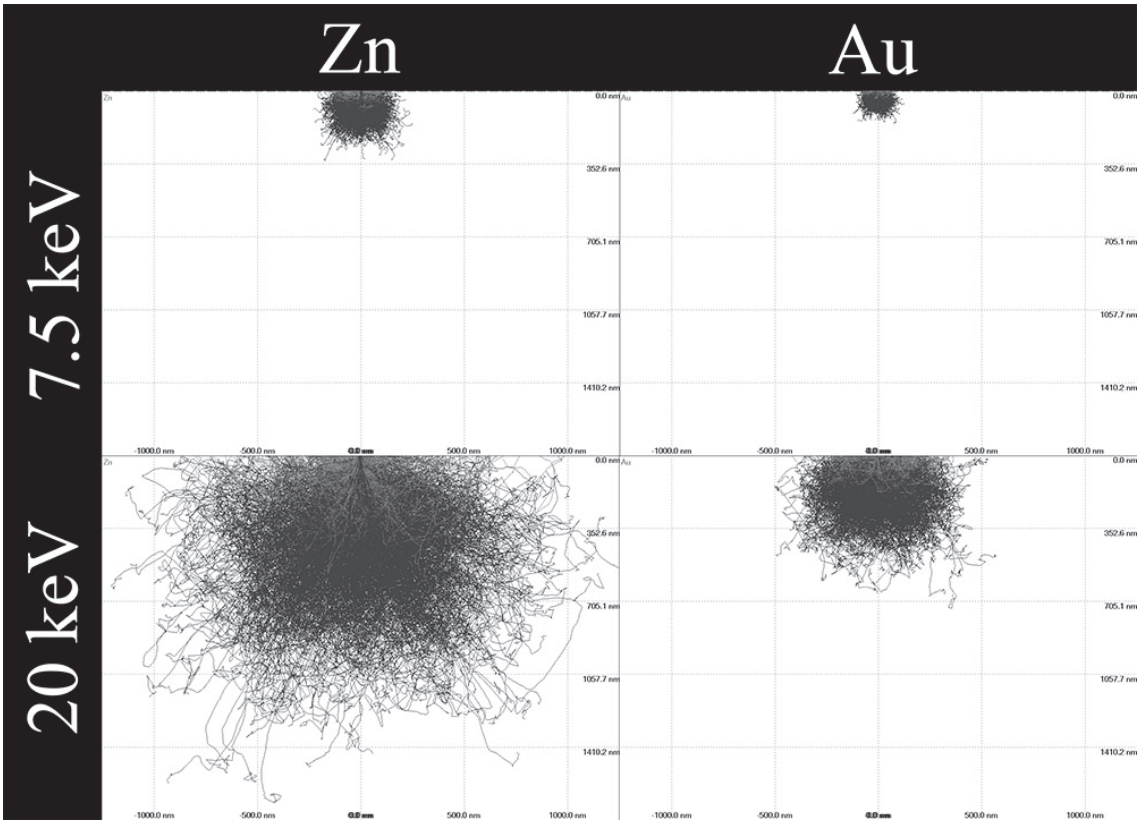

Figure 3.2 The interaction volume as a function of Z and kV**.**

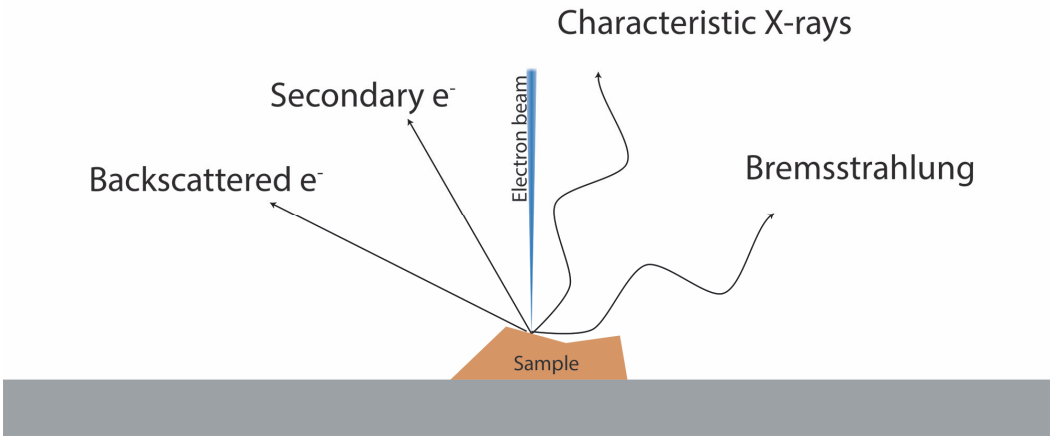

Figure 3.3 Schematic representation of some of the signals resulting from the electron – sample interactions.

3.2 Energy Dispersive Spectroscopy (EDS)

One of the signals generated from the sample as the electrons interact with it is X-ray radiation, see Fig. 3.3. Bremsstrahlung is generated when a charged particle, e.g. an electron, is decelerated. The energy of the bremsstrahlung is a continuum up to the energy of the incident electron beam. This continuum can be seen as a background signal in the EDS spectra. Characteristic X-rays are created when an incoming electron knocks out an electron from the inner shells of an atom. The vacancy created is then filled with an electron from a higher energy shell; the electron releases the excess energy in the form of an X-ray quanta. The energies for these transitions are specific for each atomic species, making it possible to determine the qualitative composition of the sample investigated. The intensities of the emitted photons are proportional to the composition of the sample; thus, making it possible to quantifiably determine the composition of the sample. The lateral resolution of the EDS analysis is determined by the width of the interaction volume [69].

For this work, two different EDS systems were employed, Oxford X-Max 80 mm^2 detector with INCA software package, and a BRUKER XFlash 6|60 detector with Quantax 1.9 software package.

3.3 Focused Ion Beam milling (FIB)

The focused ion beam (FIB) milling technique employs heavy ions to remove material from the sample. The ion beam can be focused to a small spot and scanned over the sample surface similarly to the SEM. This makes it possible to remove material in a very well defined fashion. The FIB technique is used to prepare cross sections for imaging in a SEM, as well as thin lamellae for TEM and STEM observation.

The equipment used to prepare the cross section in this thesis was a FEI Versa 3D equipped with a Ga source.

3.4 X-ray Diffraction (XRD)

X-ray diffraction (XRD) is used to determine the crystallographic characteristics of a sample. The X-ray diffraction pattern is obtained by using a diffractometer, which uses an X-ray tube in order to generate X-rays that hit the sample and are reflected towards a detector.

The X-rays interact with the sample and are scattered by the atoms in the material. There is a multitude of scattering processes that occur when the photons interact with the sample [70] For crystal diffraction, it is convenient to see the scattering as reflection from atomic planes in the crystal, due to the wave nature of the X-ray photons, see Figure 3.4. Using Bragg's law, equation 3.1, the spacing of the atomic planes in the crystal can be determined by measuring where the peaks appear in the diffractogram.

$$2dsin(\theta) = n\lambda \tag{3.1}$$

Here θ is the angle between the incoming X-ray beam and the sample surface, λ is the wavelength of the radiation, *n*- is an integer (diffraction order), and d is the interplanar spacing. The planes with the largest spacing will thus have a reflection at the smallest angles [71]. By comparing the peak positions to reference spectra, the analyzed, crystalline compound can be identified.

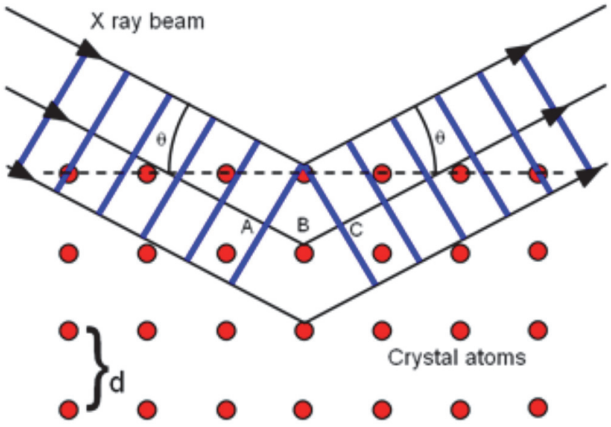

Figure 3.4 Schematic figure of the geometry of the scattering of X-rays from atomic planes.

3.5 Fourier Transform Infrared Spectroscopy (FT-IR)

FT-IR spectroscopy was used as a complement to SEM/EDS for identification of corrosion products. For local investigations, a Varian 6000 spectrometer equipped with a UMA 500 microscope using a 50μm^2 aperture was used. The spectra were collected in the region 4500 – 450 cm^{-1}. Bulk characterization was performed by an Attenuated total reflection (ATR) accessory attached to a Perkin-Elmer Frontier machine.

4. Experimental

4.1 Material

4.1.1 Substrate

Commercial grade EDT structured hot dipped galvanized steel with a zinc coating thickness of 7 μm was used. The size of the samples was 10 x 20 cm. The composition of the zinc coating is presented in Table 4.1, which is taken from paper 2, and was measured by EDS. The results were obtained at 7,5keV and 20keV corresponding to a more surface sensitive and to a more bulk-like composition, respectively. Carbon is not presented in Table 4.1, although it was included for the calculation performed by the software. This was due to the deposition of carbon on the samples during the analysis period. The measurements were obtained after degreasing the samples in an ultrasonic bath. This occurred in three steps using heptane, acetone and ethanol. The appearance of the substrate is shown in Figure 4.1, designated as "degreased," showing the structured zinc surface with plateaus and troughs.

Table 4.1 Composition of the HDG substrate. The data is an average of 80 analyses for 7,5 keV and 100 analyses for 20 keV. The results are presented as at %. The label "trace" means < 0,05 at %

Acc. Voltage	*O*	*Al*	*Si*	*P*	*S*	*Ca*	*Fe*	*Ni*	*Zn*	*Zr*
7,5 keV	*10,4*	*3,6*	*0,1*	---	---	---	---	---	*85,9*	*0,1*
20keV	*8,0*	*2,9*	*0,1*	*0,1*	*0,1*	*0,1*	*1,3*	*0,1*	*87,3*	*Trace*

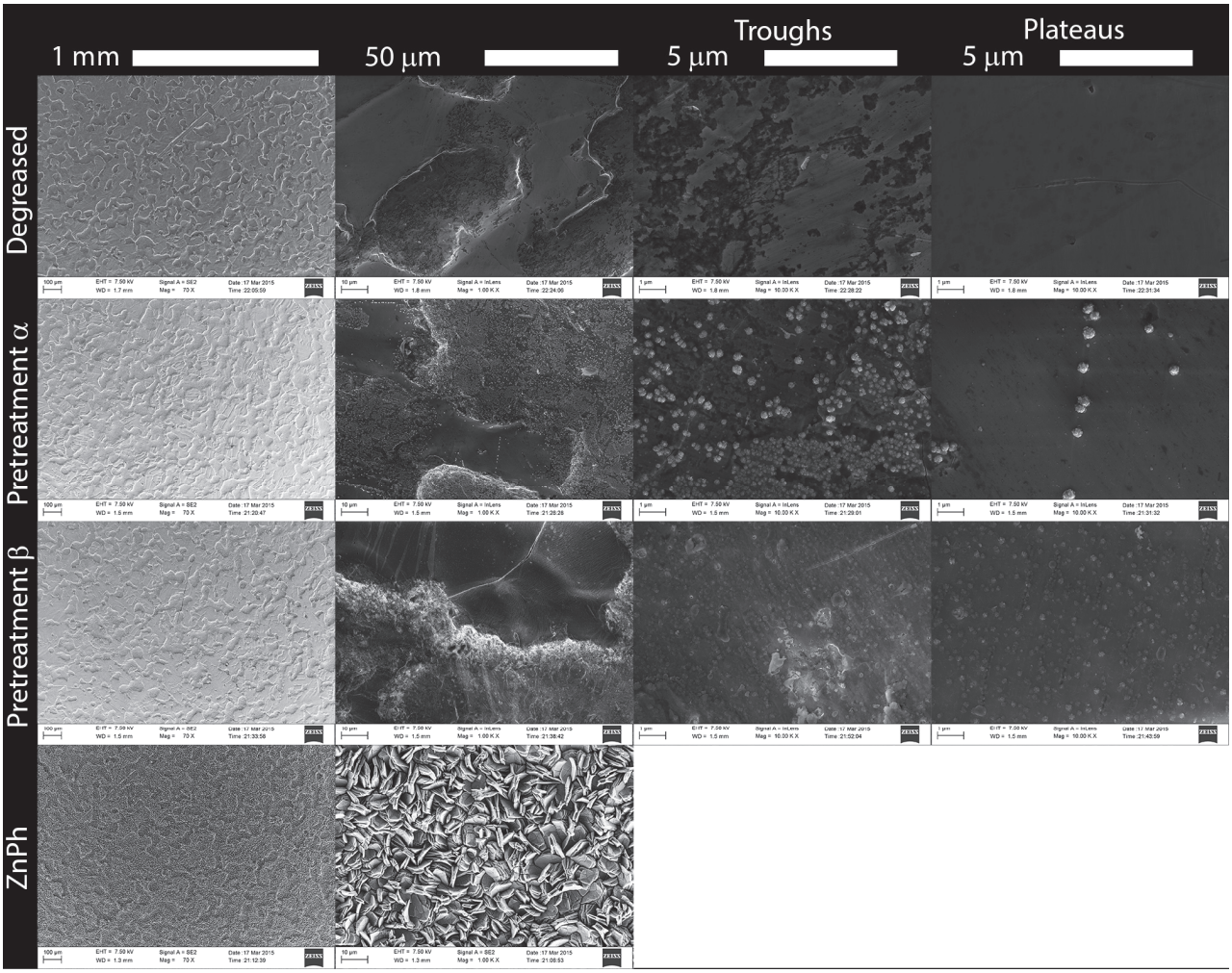

Figure 4.1 Overviews of the samples used for this work.

4.1.2 Pretreatments

Four different pretreatments were investigated: two different thin film pretreatments designated α and β, zinc manganese *phosphate* and "*only degreased"*. The α pretreatment was applied at a spray application line. The panels were hung on hooks and run through the pretreatment line, as shown in Figure 4.2. The β pretreatment was applied by dipping during running production at an automotive plant. The panels were mounted in the window frame of the car bodies going through the pretreatment line

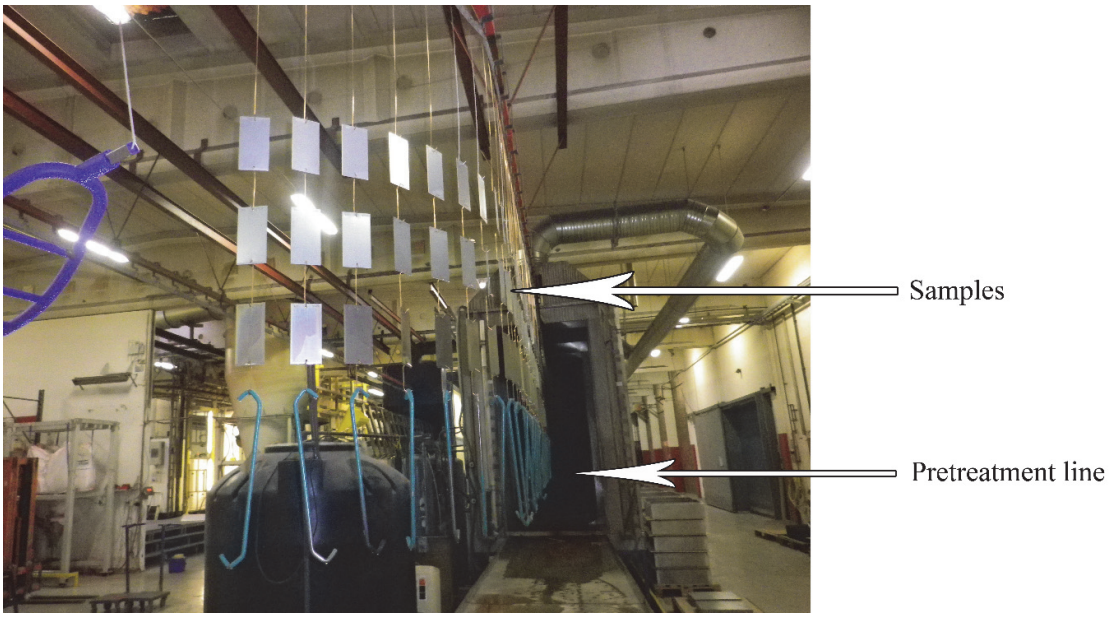

Figure 4.2 Samples coming out from a spray pretreatment line.

The conventional zinc manganese phosphated samples were pretreated at the Torslanda plant (VCT) at Volvo Car Corporation in Gothenburg, Sweden by dipping. The panels were mounted on fixtures hung from the back of V/XC70 car bodies, Figure 4.3. The “degreasing” pretreatment was performed in the lab by submerging the samples in three different solvents, heptane, acetone and ethanol, for 5 minutes. Ultra-sonic agitation was used. After each step, the samples were dried using a hairdryer.

Figure 4.3 Samples mounted on car body. Similar setups were used for phosphating of samples and for E-coating.

4.1.3 Paint system

All samples were E-coated at the paint shop at the VCT plant. The samples were mounted in fixtures that were hung on the back of V/XC70 car bodies, Figure 4.4).

The surfacer, basecoat and clearcoat were applied in the lab. The total paint thickness was 131 μm on average.

4.1.4 Scribing

In accordance with Volvo Car Standard 1021,29, the samples were scribed using a flat tool with a width of 0,5 mm (see Figure 4.5) [72]. The scribe was performed to induce damage that reached down to the steel, see Figure 4.6. The purpose of this was to initiate underpaint corrosion. It should be noted that, during the scribing process, the "only degreased" sample showed signs of paint chipping off from the substrate close to the scribe.

Figure 4.5 Scribing the samples using a scribing tool.

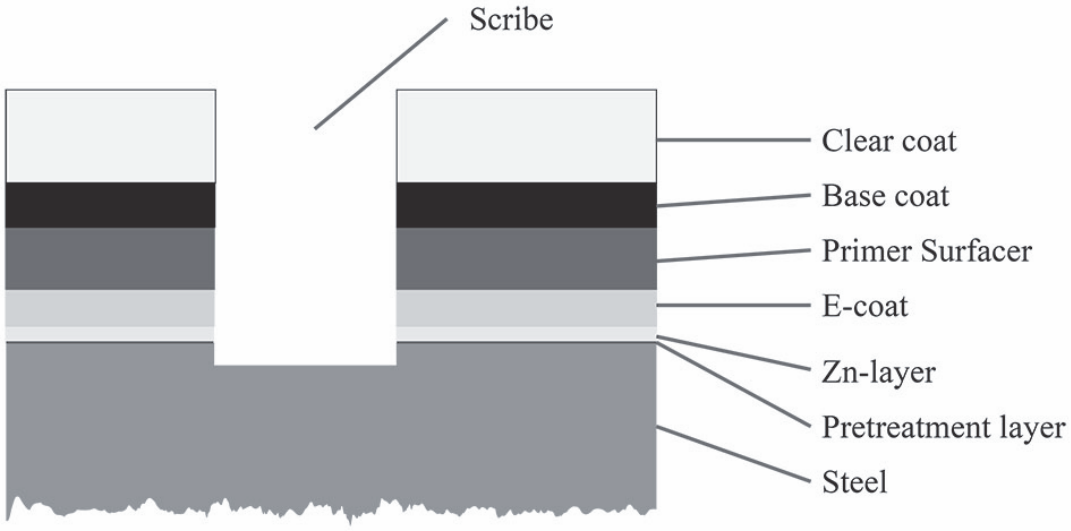

Figure 4.6 Schematic cross section of a sample. Layers not to scale.

4.1.5 Corrosion exposure

The samples were exposed for three weeks to a cyclic accelerated corrosion test procedure developed by Volvo Car Corporation, ACTII [73]. The corrosion test operated in 168h cycles and included cycling of temperature (25-50°C) and humidity (70-95% RH). During the wet periods, rain was simulated three times by spraying a 0.5 wt% NaCl solution on the panels. The weekly cycle is shown in Figure 4.7. The last "rain" in each cycle was substituted by spraying the samples by hand with an aqueous solution, containing 0,321M KCl and 0,107M NaCl. The addition of KCl was used because potassium does not have any overlapping peaks in the region of interest in the EDS spectrum, as opposed to sodium that has an overlap with the Na K and Zn L peaks. The chemistry of the potassium is expected to be similar to the sodium in this context. Selected samples were subjected to the cyclic test for 504 and 2184 hours.

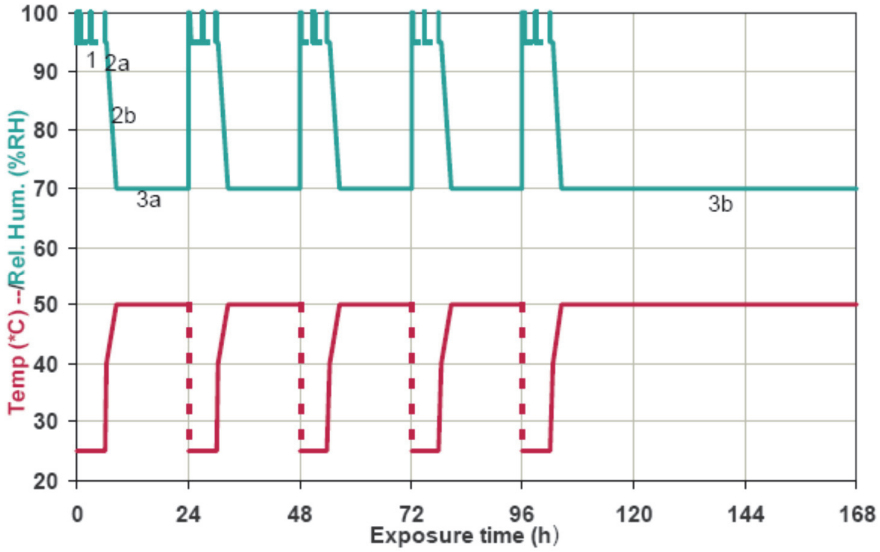

Figure 4.7 Overview of the weekly ACTII cycle [73].

4.1.6 Post exposure analysis

Before paint removal

After removing the samples from the corrosion cabinet, imaging by optical stereo microscope (Wild M8) was performed. The corrosion blisters were measured using image J software.

Corrosion products that had leaked out from the blisters were scraped off with a scalpel and analyzed with FT-IR ATR (Perkin Elmer Frontier) in the wave number range 4000 – 450 cm^{-1}. The spectra were analyzed with Spectra software and compared to standards.

Evaluation of underpaint creep

The determination of underpaint creep was performed according to the Volvo Car Corporation standard VCS 1021,29 [72]. The underpaint creep is determined by dividing the scribe into five segments of equal length, disregarding 10 mm at each end, see Fig. 4.8. The

paint creep is then determined by averaging the values of the total delamination in each segment. As shown in eq. 4.1, the scribe itself was not counted.

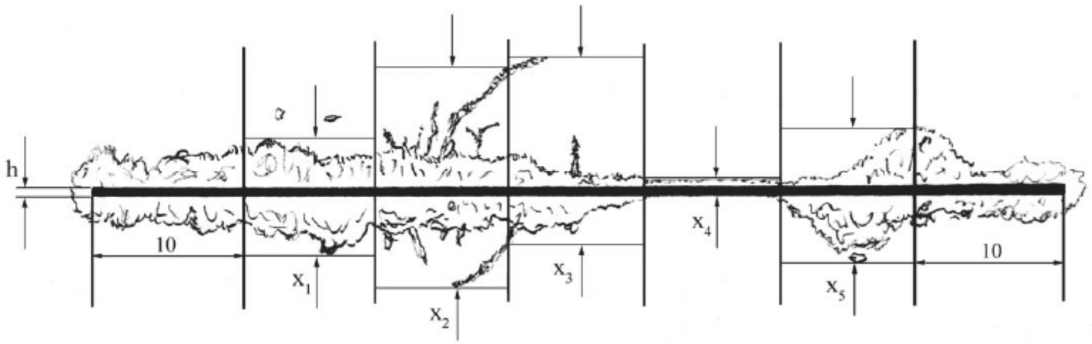

Fig. 4.8 Schematic view of segmentation of scribed, corroded samples for underpaint creep determination.

$$Underpaint\ creep\ distance = \frac{\sum_{n=1}^{5}(x_n - h)}{5} \quad (4.1)$$

Cross sections

Cross sections were prepared selected samples. The samples were cut into smaller pieces using a band saw and embedded in epoxy resin (Epofix, Struers) in a vacuum chamber. They were left to cure overnight. The embedded samples were then ground until they were planar using SiC paper and polished to 1 μm finish using diamond spray (DP-Spray, Struers) and an oil based lubricant (DP-Yellow, Struers). The polished samples were then imaged using SEM, see below.

Paint removal

Using a band saw, 1 x 1 cm squares that included the scribe and representative blisters were cut from the samples. The paint system was then removed using n-methylpyrrolidon (Merck, Germany) at 80-90°C until the paint was removed from the substrate. The samples were then rinsed with ethanol and dried using a hairdryer.

XRD

After paint removal, the samples were investigated using a Bruker D8 X-ray powder diffractometer. The X-ray source was fixed at 2° and the detector was scanned between 10° - 80°. The diffractograms were compared to pdf-cards using Bruker EVE software in order to determine the crystalline products present.

SEM/EDS investigation

Prior to corrosion exposure, the pretreated samples were imaged using a Leo Ultra 55 FEG-SEM using an accelerating voltage of 7,5 keV. The samples were then analyzed using a Bruker Quantax 6|60 EDS detector and Esprit 1,9 software. The EDS system was attached to

a Zeiss EVO MA15 SEM with a LaB_6 emitter. The EDS analysis was performed using an accelerating voltage of 7,5 and 20 keV over 80 and 100 areas (approximately 1,5 x 1 mm each), respectively. Some areas were removed as they were contaminated by fibers and particles.

The corrosion blisters were imaged from a top down perspective using both a FEI Quanta 200 FEG-SEM and the previously mentioned Zeiss EVO machine. In order to avoid coating the samples, the imaging was performed at 0,6 Torr pressure to neutralize charge up. The accelerating voltage used was 20 keV. EDS analysis was performed using both an Oxford XMax 80 detector with INCA software attached to the FEI machine, as well as the previously mentioned Bruker system. All EDS analyses were done by standardless methods. The acquisition time using INCA was 60 seconds per spectra. The spectra obtained by the Bruker system were obtained until the number of counts reached 1 000 000.

The polished samples were imaged and analyzed by EDS at 0,6 Torr and 20 keV. Ag paint was applied around the area of interest and care was taken to achieve electrical contact with the steel substrate.

FT-IR

Local FT-IR analysis near the corrosion front was performed using a Varian 7000 spectrometer equipped with a UMA 500 microscope. The size of the aperture and, thus, the analyzed area was 50x50 μm. The wave number range was 4500 – 450 cm^{-1}. The data was analyzed using Perkin Elmer Spectrum software.

5. Results

5.1 Blister morphology and underpaint creep

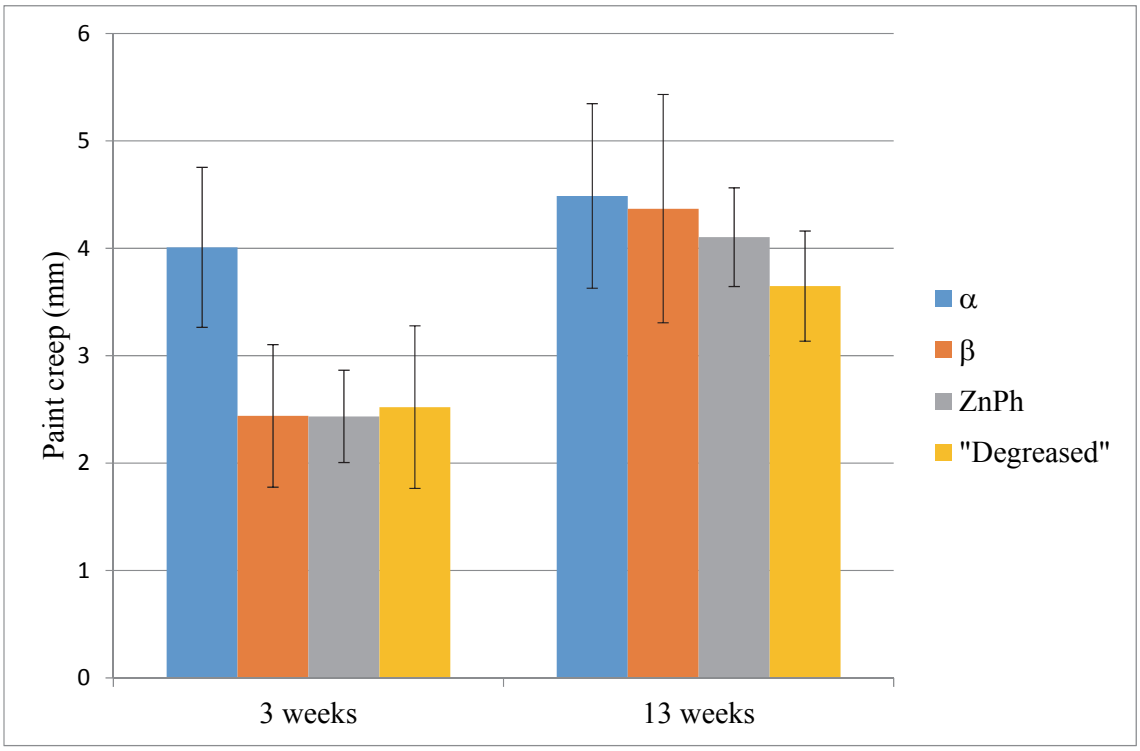

Fig. 5.1 The extent of underpaint corrosion for samples exposed for 504h and 2184h, showing the standard deviation of the results.

The underpaint delamination distances are shown in Fig. 5.1 for both 504h and 2184h exposures. With the exception of the β material, which had larger delamination than other materials after 504h of exposure, all samples showed similar delamination.

The optical micrographs in Fig. 5.2 illustrate the entire scribe after the corrosion exposure for 504h (left side) and 2184h (right side). The underpaint corrosion attack manifested itself as blisters. On all four types of samples the blisters were roughly semicircular and centered on the scribe. After 504h the blisters on the phosphated material exhibited a characteristic morphology wherein a central or primary blister was surrounded by several secondary blisters. In contrast, the two thin film pretreated samples and the “only degreased” material did not form secondary blisters at this stage, see left side of Fig. 5.2.

Similar blistering was also observed after 2184h, see the right hand side of Fig. 5.2. The main difference was that all materials exhibited secondary blistering at this stage. However, secondary blistering was absent on the larger blisters on the “only degreased” material. It may be noted that more red rust had formed in the scribe after 2184h compared to 504h.

Figure 5.2 Light optical micrographs of the scribes of all samples, after 504h (left) and 2184h (right) corrosion exposure.

5.2 Analysis of the scribe

In Fig. 5.10, the scribe of a α sample after 2184h exposure is shown. The SEM micrograph is overlaid with the element map for sodium. One can see that, in some areas, the scribe have an enrichment of sodium. This was the case for all samples.

The sodium enrichment in the scribe indicates the presence of a cathodic area where oxygen reduction occurs. The cathodic areas do encompass only parts of the scribe rather than the entire area.

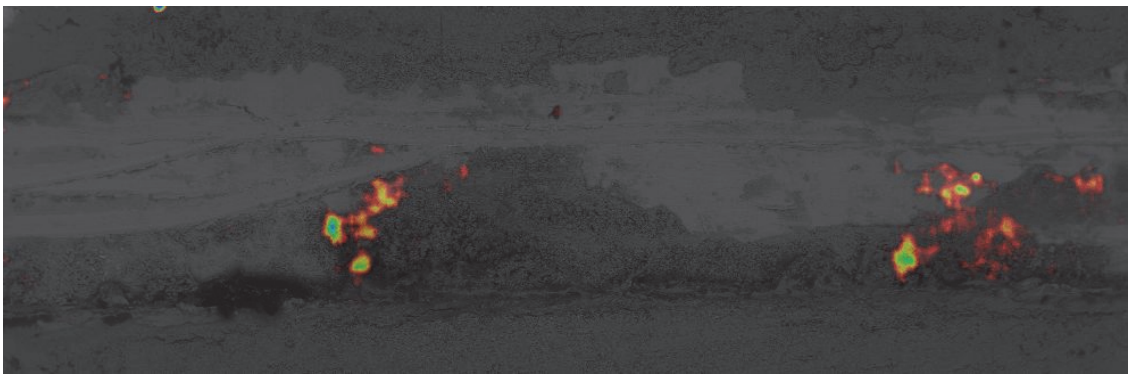

Figure 5.10 A micrograph of the scribe area of an α pretreated material after 2184h exposure with the sodium signal overlaid in red.

5.3 Analysis of the corrosion blisters

After exposure, all sample types exhibited white areas on the paint surface in the vicinity of the scribe, see Fig. 5.2. Analysis by FT-IR ATR showed that, in varying proportions, the deposit consisted of hydrozincite and simonkolleite, see Fig. 5.3.

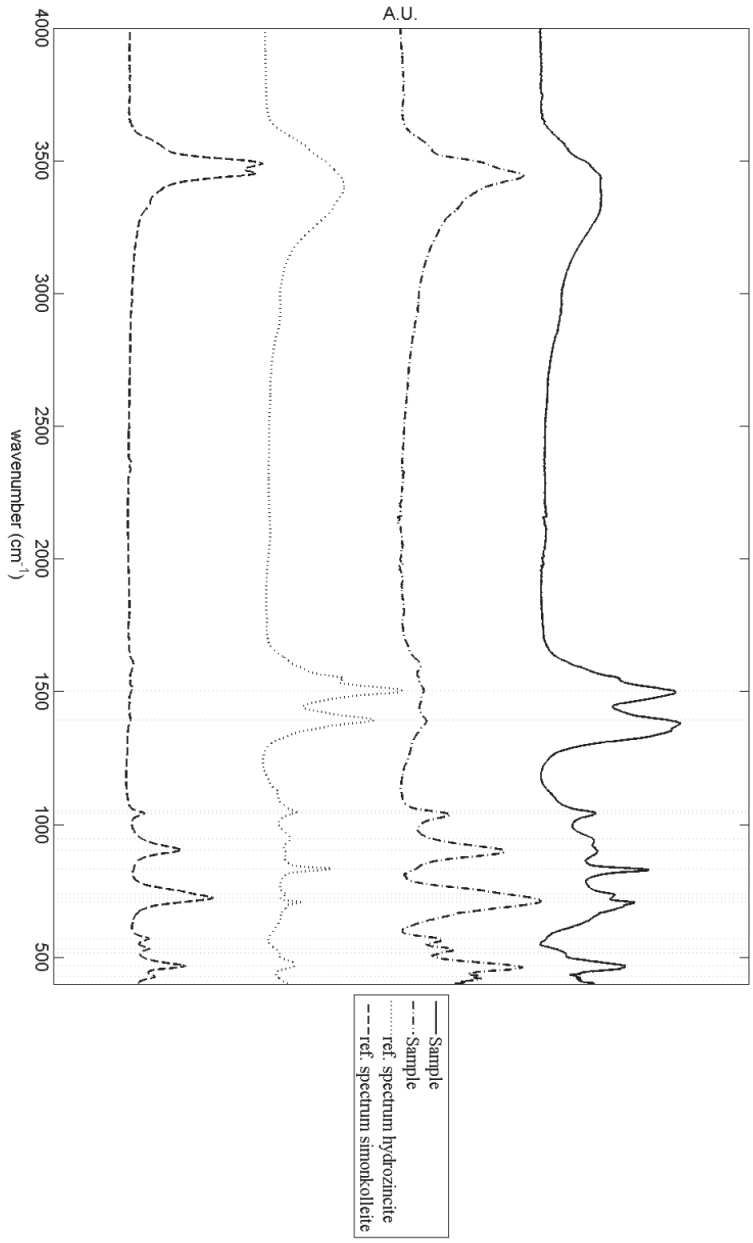

Figure 5.3 FTIR-ATR analysis of white corrosion products on the paint surface (the two upper spectra). The two bottom spectra (dotted and dashed) are reference spectra for hydrozincite and simonkolleite respectively.

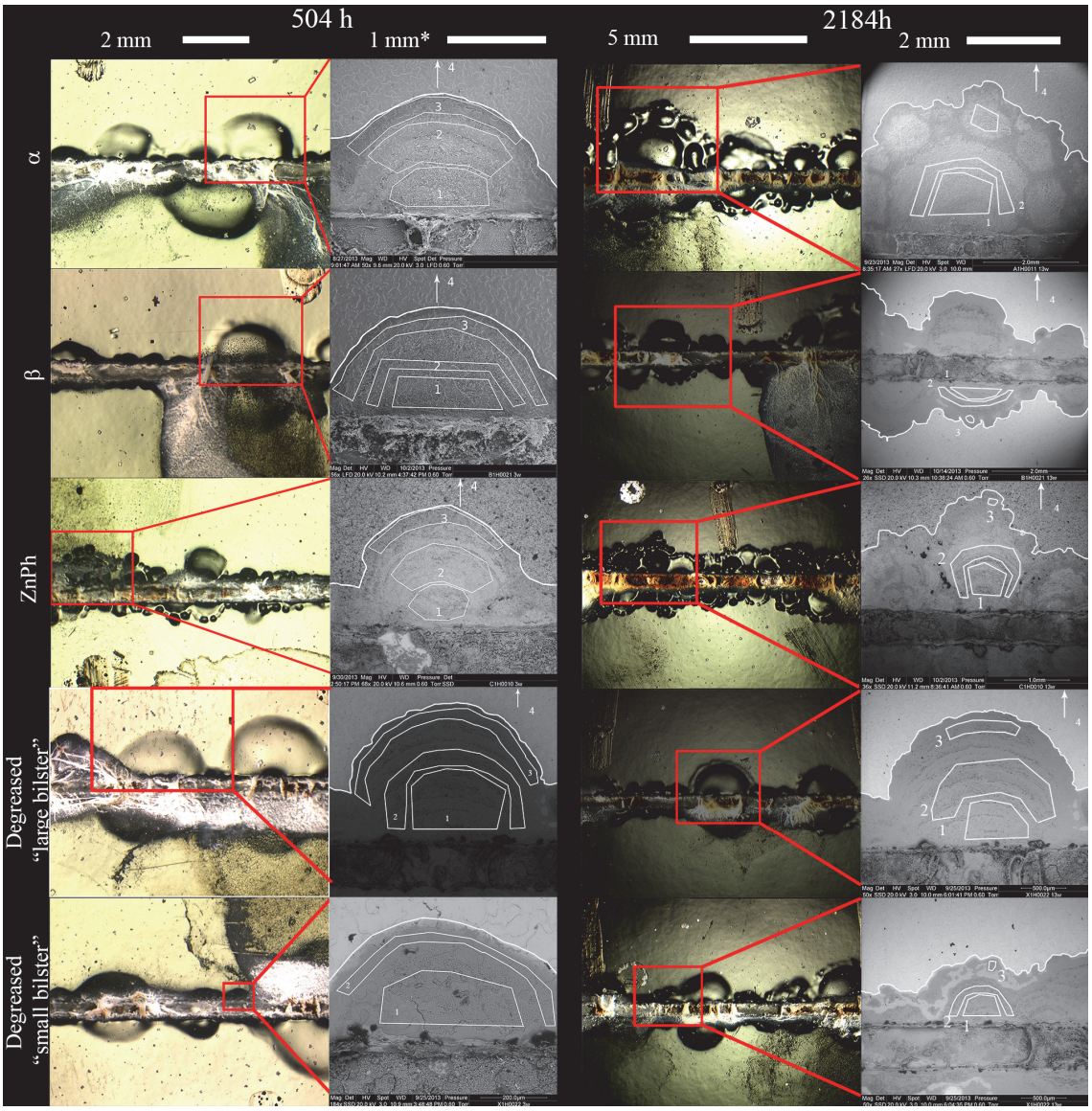

Figure 5.4 Light microscopy images of the corroded samples (504h exposure on the left hand side and 2184h on the right hand side) and corresponding SEM images after paint removal. The samples were phosphated, α and β pretreated and "only degreased", respectively. The two rows of images of the "only degreased" samples show large and small blisters, respectively. The (horizontal) scribe is at the bottom of the SEM micrographs and the extent of the blistered area is indicated by the thick white line. *In the bottom row SEM image (small blister, only degreased exposed for 504h), the scale bar corresponds to 300µm.

The two columns to the left in Fig. 5.4 show samples exposed for 504h, before and after paint removal. The two columns to the right show samples exposed for 2184h. EDS data from the regions indicated in Fig. 5.4 are presented in Tables 5.1 and 5.2. The analysis suggests that the main corrosion product in the blister is simonkolleite. It is worth mentioning that no sodium was detected in the blistered area on any samples. The lack of sodium and presence of chlorine near the corrosion front suggests that the zinc has dissolved by an anodic process with the cathodic process occurring in the scribe, as mentioned previously. One can also argue that the blister is separated from the environment not only by the paint layer, but also

by a porous mass of corrosion products. This porous mass of corrosion products prevents the mixing of the electrolyte in the scribe with the electrolyte in the blister, as evidenced by the lack of sodium inside the blister. It is suggested that this separation between the environment inside the blister and the environment outside the blister causes an osmotic pressure to build up, resulting in the observed semicircular blisters.

Table 5.1: EDS analysis of blistered areas after 504h of exposure. The areas analyzed are indicated in Fig. 5.4. For all materials, "area 4" represents a non-corroded part of the surface, far from the blister. The carbon content is not included.

α

Area	1	2	3	*4*
O	48,2	48,5	48,1	4,7
F	0,1	0,1	0,2	----
Al	0,9	0,9	1,1	3,3
Si	0,2	0,2	0,1	0,4
P	----	----	----	0,4
S	trace	----	trace	1,3
Cl	15,6	15,1	14,8	----
Fe	3,4	3,2	2,8	----
Ni	0	0	0	0,2
Zn	31,5	32	32,8	73,5
Zr	0	0	0,1	0,7
Zn/Cl	2	2,1	2,2	N/A

β

Area	1	2	3	4
N	4,4	4,6	4,3	----
O	46	46	45	19
F	----	----	----	0,3
Al	0,7	0,8	1,4	2,9
Si	----	trace	trace	0,2
P	----	----	----	0,4
Cl	15,4	14,5	13,4	0,3
Fe	2,3	2,1	2	1,4
Zn	31,2	31,8	33,8	73,7
Zr	trace	0	0,2	1,7
Zn/Cl	2	2,2	2,5	273

ZnPh

Area	1	2	3	4
O	53,3	53,9	56,6	55,6
Al	0,6	0,8	0,8	0,6
Si	trace	trace	trace	0,2
P	2,2	4	8,8	14,4
Cl	11,4	10,8	6,5	----
Ca	trace	trace	trace	----
Ti	trace	trace	0,1	0,2
Mn	0,2	0,3	0,8	1,7
Fe	2,8	2,2	1,7	0,7
Ni	0,1	0,1	0,2	0,4
Zn	29,3	27,7	24,4	26,2
Zn/Cl	2,6	2,6	3,7	N/A

"Degreased" (large blister)

Area	1	2	3	4
O	49,9	49,4	46,9	8,4
Al	0,8	0,9	1,1	3,1
Si	trace	0,1	trace	
P	0,1	0,1	0,2	0,2
S	trace	trace	trace	
Cl	15,4	14,9	14,1	
Fe	1,6	1,6	1,5	1,5
Ni	trace	trace	trace	
Zn	32,1	33	36,2	86,8
Zr				trace
Zn/Cl	2,1	2,2	2,6	N/A

"Degreased" (small blister)

Area	1	2
O	47,3	44,2
Al	1,4	1,6
Si	0,1	0,2
S	trace	trace
Cl	13,4	12,3
K	0,1	0,1
Ca	0,1	trace
Ti	0,1	0,1
Fe	1	0,8
Ni	trace	trace
Zn	36,5	40,5
Zr	trace	0,1
Zn/Cl	2,7	3,3

Table 5.2: EDS analysis after 2184h exposure. The areas analyzed are indicated in Fig. 5.4. "Area 4" represents a part of the surface showing no corrosion, far from the blister. The carbon content is not included

Pretreatment α

Area	1	2	3	4
N	4,4	4	4,1	5,1
O	48,8	48,9	46,8	15,9
Al	0,2	0,5	0,7	2,9
Si	0,1	trace	trace	0,1
P	trace	0,1	0,1	0,2
S	trace	Trace	0,2	----
Cl	13,3	12,3	10,6	----
Fe	2	1,7	1,9	1,8
Ni	----	----	----	0,1
Zn	31,3	32,5	35,7	73,1
Zr	----	----	----	0,7
Zn/Cl	2,4	2,6	3,4	N/A

Pretreatment β

Area	1	2	3	4
N	4,7	4,4	4,6	4,5
O	46,8	46,6	44,8	19,8
F	trace	0,1	trace	----
Al	0,4	0,6	0,9	3
Si	0,1	0,1	0,1	0,4
P	----	----	----	0,3
Cl	14	13,2	12,9	----
Fe	1,6	1,3	1,6	1,2
Ni	----	----	----	trace
Zn	32,4	33,7	34,8	69
Zr	0	0,1	0,3	1,7
Zn/Cl	2,3	2,6	2,7	N/A

ZnPh

Area	1	2	3	4
O	49,7	50,9	52,1	54
Al	0,2	0,3	0,2	0,5
Si	trace	trace	0,1	0,1
P	1,3	3,4	5,4	13,8
Cl	14,4	12,5	10,8	0,4
K	0,1	0,2	0,2	trace
Ti	0,1	0,1	0,2	0,2
Mn	0,1	0,1	0,3	1,5
Fe	1,2	1,3	0,7	0,8
Ni	0,1	0,1	0,1	0,4
Zn	32,9	31,1	29,7	28,4
Zn/Cl	2,3	2,5	2,7	72,2

"Degreased" (large blister)

Area	1	2	3	4
O	47,9	46,9	45,1	8,4
Al	0,6	1	1,1	2,8
Si	----	0,2	traces	0,3
Cl	15,9	15,5	15	0,5
Ti	trace	trace	----	trace
Fe	1,7	1,6	1,6	1
Ni	----	trace	trace	trace
Zn	33,8	34,8	37,1	86,9
Zr	trace	trace	trace	0,1
Zn/Cl	2,1	2,2	2,5	180,8

"Degreased" (small blister)

Area	1	2	3	4
O	46,7	46,8	44,7	8,4
Al	0,2	0,4	0,4	2,8
Si	0,1	0,3	0,1	0,3
Cl	14,2	14,5	13	0,5
Ti	0,1	trace	0,1	trace
Fe	1,4	1,2	1,2	1
Ni	trace	----	----	trace
Zn	37,4	36,8	40,4	86,9
Zr	----	trace	----	0,1
Zn/Cl	2,6	2,5	3,1	180,8

In the center of the blistered area of the ZnPh pretreated materials, corrosion products form agglomerates consisting of <0,5 μm thick plate-like crystals, see Fig. 5.5. The other materials exhibited alternating large and small crystals, as seen in Fig. 5.5. Despite the difference in morphologies, EDS data showed that the corrosion products were indeed simonkolleite.

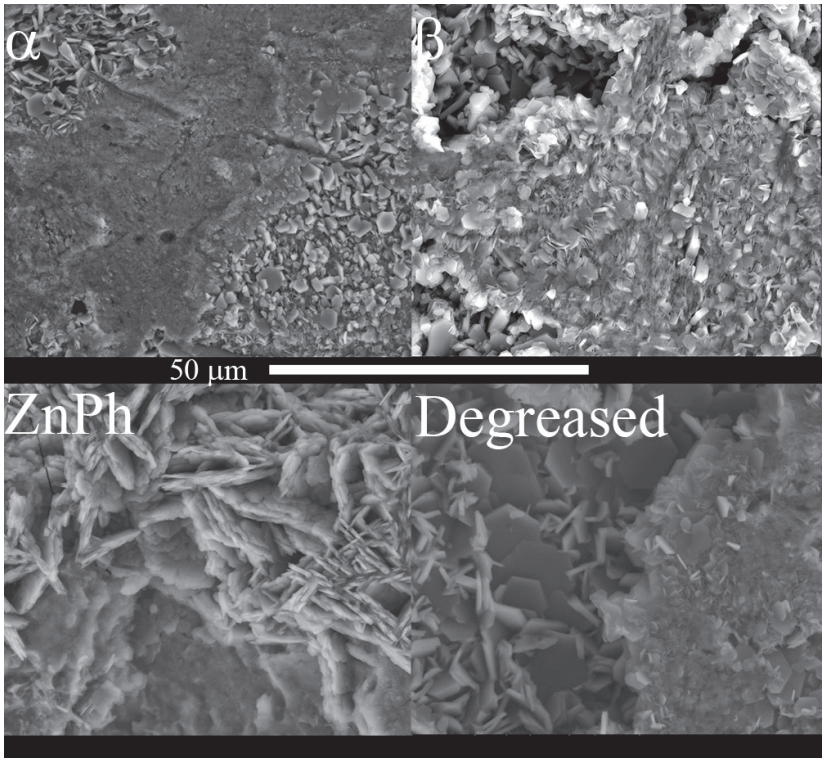

Figure 5.5 Higher magnification SEM micrographs of the central part of blister.

The X-ray diffractogram shown in Fig. 5.6 corroborated the results obtained from the EDS data by showing that the main crystalline corrosion product was simonkolleite ($Zn_5Cl_2(OH)_8 \cdot H_2O$). On the α and "only degreased" samples after 504h exposure, there was an unidentified peak $2\theta=12.35°$. This peak was stronger for the "only degreased" material than for the β pretreated ones. After 3 months in a desiccator, the peak had decreased substantially in intensity. The peak was not present on samples exposed for 2184 h.

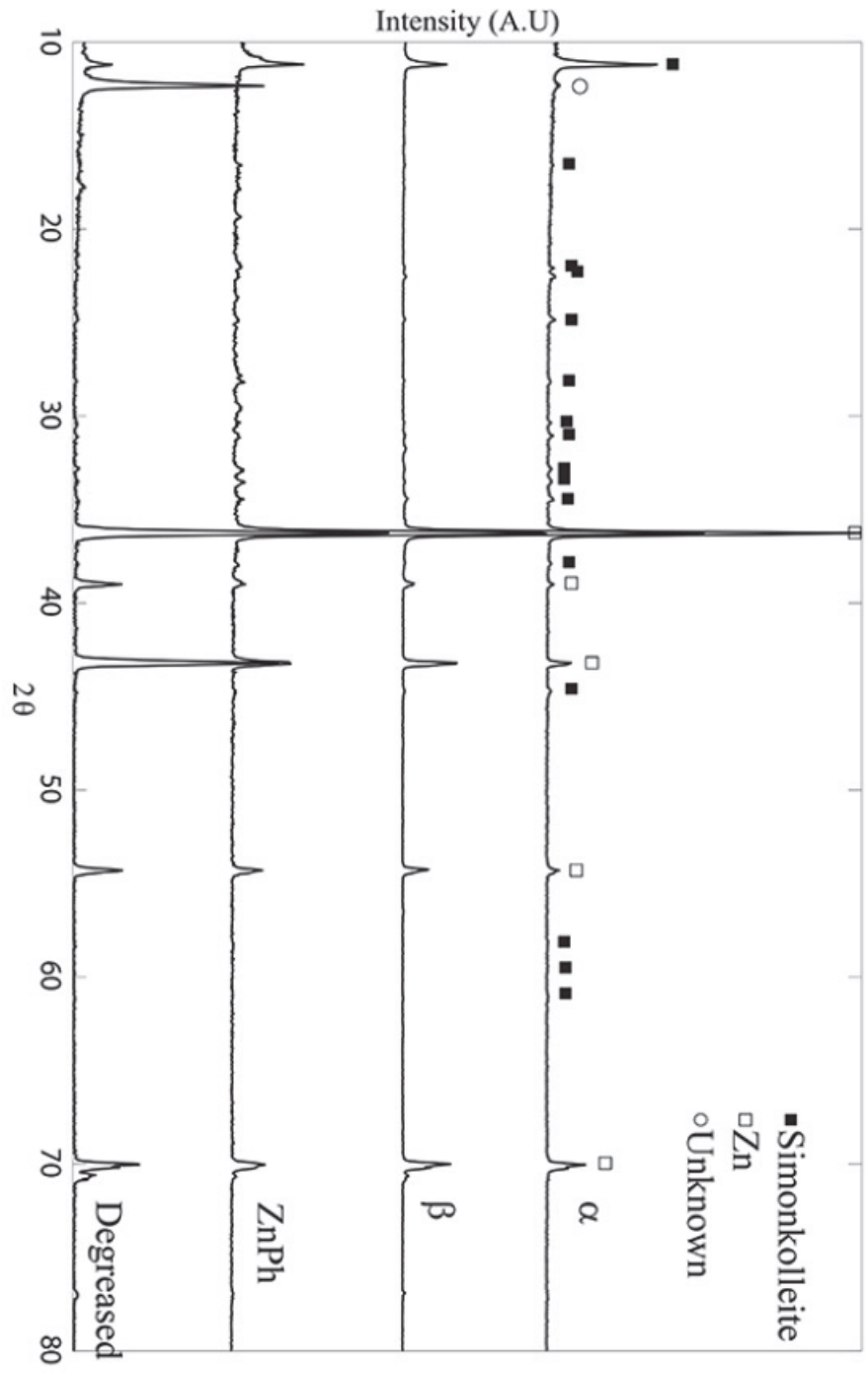

Figure 5.6 XRD diffractograms after corrosion exposure and paint stripping.

5.4 Investigation of the corrosion front

Fig. 5.7 shows micrographs of the corrosion front for all materials, as well as a mapping of the Cl signal. The left column shows samples exposed for 504h; the right one shows samples exposed for 2184h. After 504h, the images at higher magnification (middle column), as well as the Cl maps (right column) show grain boundary corrosion for the α, β pretreated, and "only degreased" materials. The preferential attack of grain boundaries in the zinc layer produces an archipelago-like structure. This structure is mostly visible in the troughs. This is due to the higher number of grain boundaries in the troughs as compared to the plateaus. In the micrographs with higher magnification, one can also observe the presence of metallic zinc grains, which are embedded in the corrosion products and visible as light gray spots. The nature of the corrosion front on the phosphated material was obscured by the phosphate layer. The smaller blisters on the "only degreased" material do not show any grain boundary corrosion, but rather a gradual transition between the corroded and non-corroded areas, as evidenced by the gradual change in chlorine signal in Fig. 5.7. Corrosion fronts of the materials exposed for 2184h are shown in the right column of Fig. 5.7. The images show that the corrosion front morphology is similar. Although, it is slightly more blurred when compared to the material exposed for 504h.

Fig. 5.8 shows FIB cross sections at the corrosion front (corresponding to the border between the blister and the non-corroded surface) for the β pretreated material. Both troughs and plateaus are represented. The face of the remaining zinc layer is V – shaped in the through region (upper image) and is wedge shaped in the plateau region (lower image).

A detailed investigation of the corrosion front shows that the dissolution rate of zinc is not the same across the entire face of the zinc layer that has been exposed to the electrolyte. Thus, the corrosion propagates predominantly through the grain boundaries, as well as in the zinc/steel interface. It also appears that, for the trough regions, the corrosion also propagates predominantly in the zinc/pretreatment interface (Fig. 5.8, upper image). This dissolution of zinc by the chloride containing electrolyte will form $ZnCl_2$ (aq), which further promotes the dissolution of zinc. The grain boundary corrosion results in an archipelago-like structure, as seen in figure 5.7, especially for the thin film pretreated materials.

In Fig 5.8, one can see that the corrosion products are of the same thickness as the non-corroded zinc coating. This suggests that there is no pressure from the expanding corrosion products on the paint system at the corrosion front. This shows, together with the lack of corrosion products on top of the zinc, that the paint layer does not delaminate prior to the passing of the corrosion front. It delaminates after the front has passed. The delamination of the paint layer must occur when the zinc coating has corroded completely. A suggested scheme for the anodic dissolution is presented in Fig. 5.9.

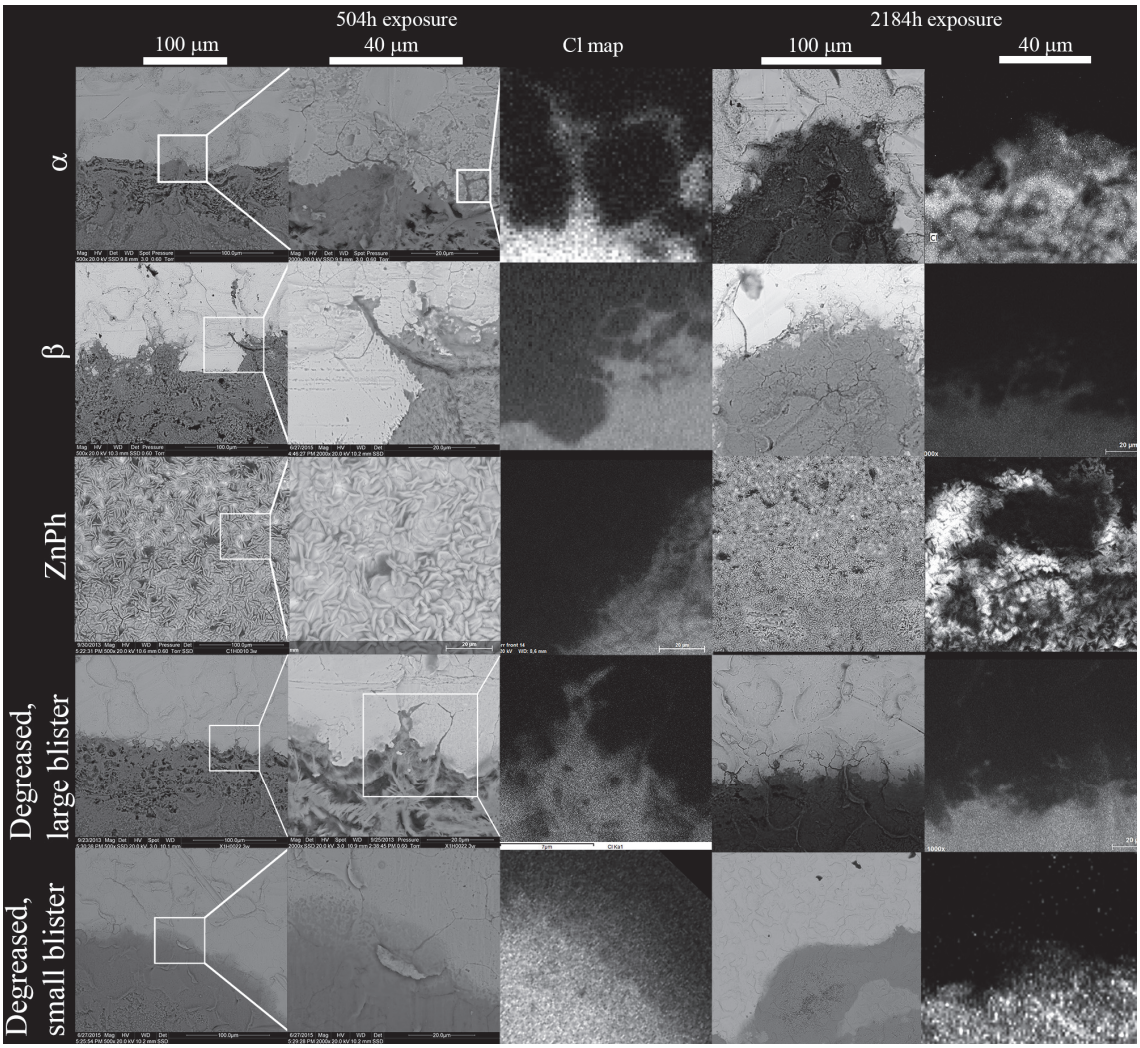

Figure 5.7 Micrographs showing representative images of the corrosion front after 504h and 2184h exposure for the two thin film pretreatments α and β, for ZnPh, and for the "only degreased" material. The corresponding EDS Cl maps are in the right hand column. The scale bar for the Cl map for ZnPh after 2184h exposure corresponds to 225 µm.

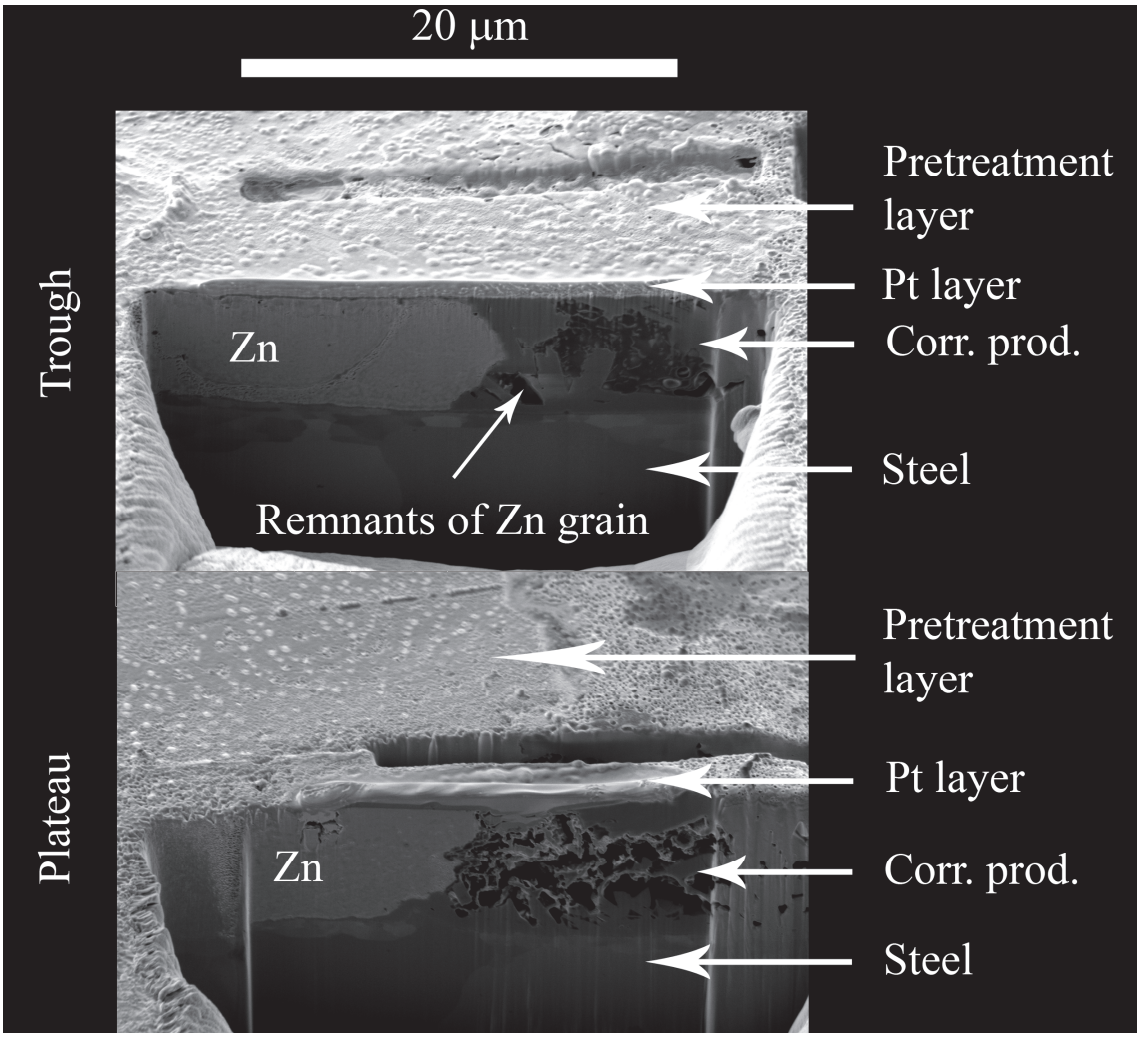

Figure 5.8 Cross sections at the corrosion front of the α - pretreated material after 504h exposure. The top image shows a trough in the zinc coating while the bottom image shows a plateau. The corrosion products show darker contrast.

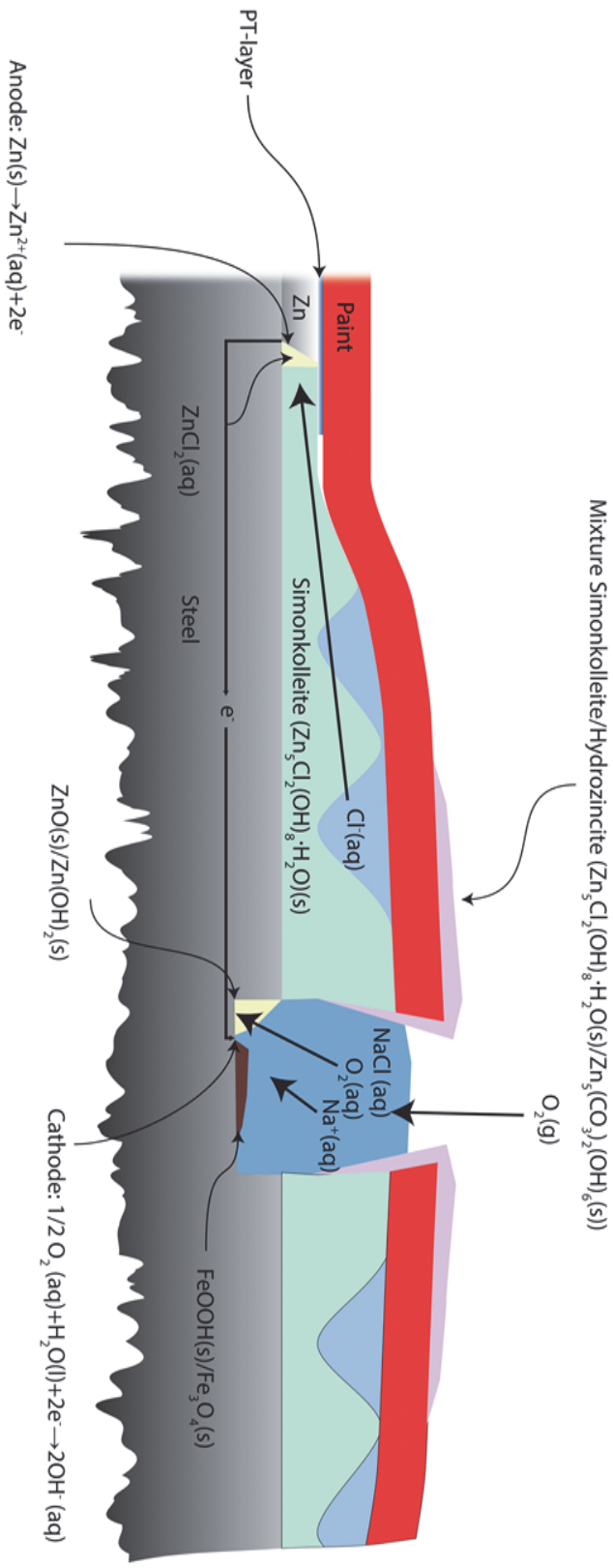

Figure 5.9 Proposed scheme for anodic undermining of paint on HDG steel during ACTII.

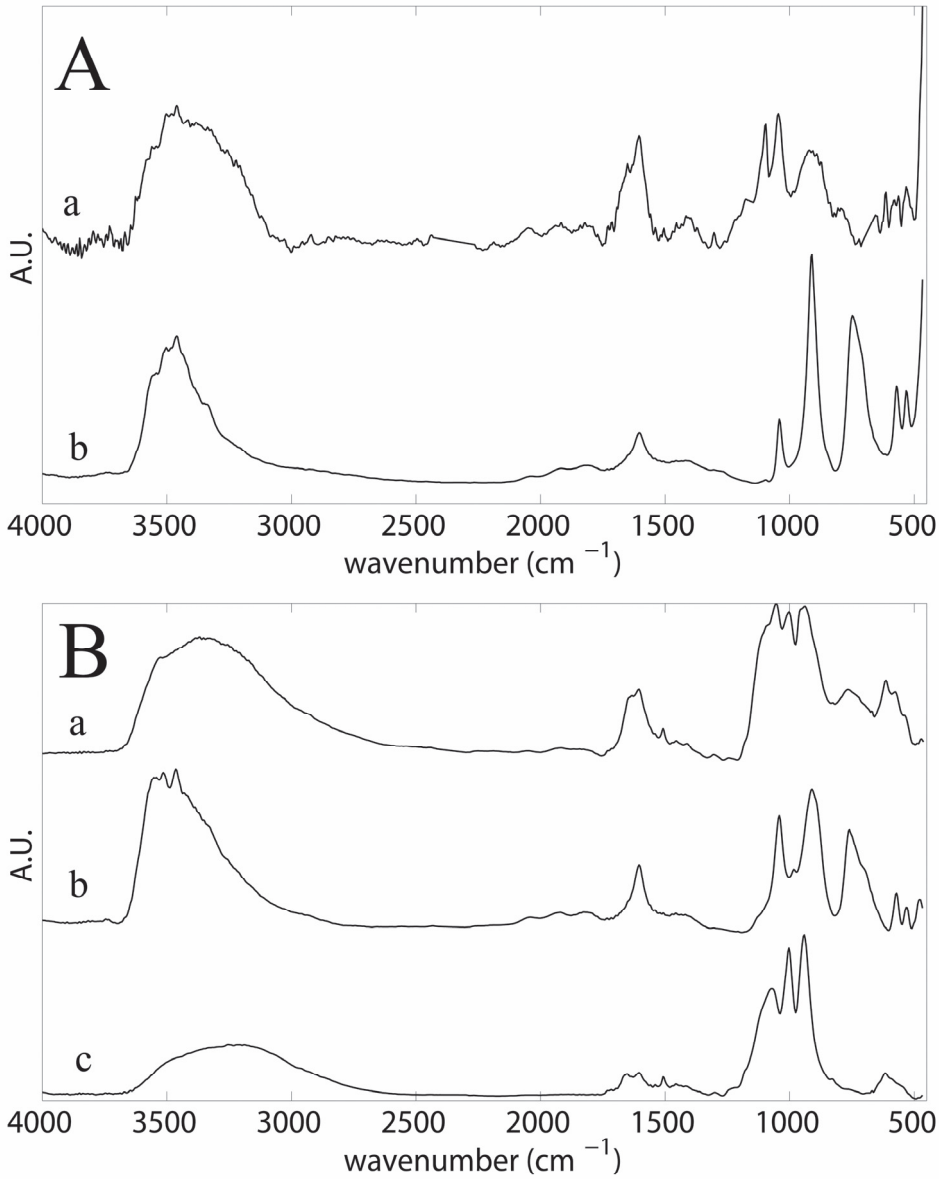

Figure 5.10 FT-IR spectra from a α pretreated sample α (*A*) and ZnPh (*B*) after 504h exposure. In diagram A, the *a* and *b* spectra are at and behind the corrosion front, respectively. In diagram B, spectrum *a* is ahead of, *b* is at and *c* is behind the corrosion front.

FT-IR spectra collected by FT-IR microscopy at different locations on all samples after corrosion exposure are shown in Fig. 5.10. The spectra obtained for the α pretreated sample are representative for all thin film and for the *"only degreased"* materials (Fig. 5.10A). The results show that the dominant corrosion products in the central part of the blister are simonkolleite for all samples. For all samples except ZnPh, the spectra suggest the presence of ε -$Zn(OH)_2$ at the corrosion front (immediately in front of the blister) [74]. The spectrum obtained from the phosphated sample, Fig. 5.10B, shows a gradual change from simonkolleite to hopeite [75] as we move across the corrosion front into the non-corroded area.

simonkolleite to hopeite [75] as we move across the corrosion front into the non-corroded area.

The detection of ε -$Zn(OH)_2$ indicates that a cathodic reaction has occurred at or near the corrosion front. This would be at variance with the previously suggested corrosion scenario with anodic dissolution of zinc at the corrosion front and reduction of oxygen in the scribe. A possible explanation is that there is a decoupling of the main cathode in the scribe during the dry periods (RH=70%) in the ACTII cycle. The electrolyte inside the blister responds slowly to the changes of the environment outside the blister and, presumably, still contains a liquid electrolyte during the dry part of the cycle. It is possible that the cathodic reaction is the reduction of small amounts of oxygen that is dissolved in the electrolyte. This reduction is occurring at or near the corrosion front. Alternatively, the decoupling of the main cathode in the scribe causes the polarization of the zinc to decrease to such an extent that hydrogen evolution becomes possible, see Pourbaix diagram in Fig. 2.1. A suggested scheme for this is presented in Fig. 5.11.

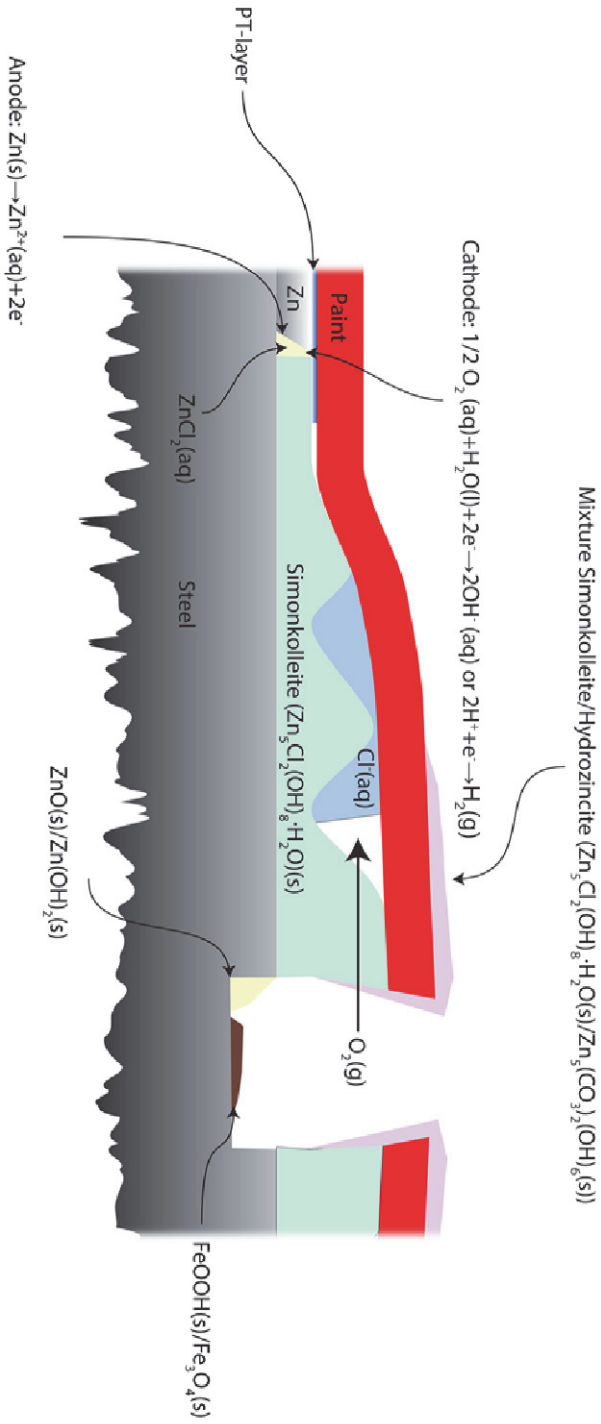

Figure 5.11 Proposed scheme for corrosion during the dry periods of the ACTII cycle.

6. Conclusions

This thesis focuses on the corrosion behavior of painted automotive galvanized steel during cyclic corrosion exposure. Four different pretreatments are compared; the traditional Zn-phosphating, two commercially available Zr-based pretreatments, α and β, and materials that where only degreased. The samples were exposed in a cyclic corrosion chamber for 504h and 2184h, respectively. The following conclusions have been drawn:

- The initial delamination mechanism was anodic undermining for all four investigated surface treatments, the Zn coating suffering anodic dissolution, and the exposed steel scribe acting as the cathode.
- The zinc layer suffered grain boundary corrosion on the thin film pretreated materials and on the "only degreased" samples.
- The face of the corroded zinc was wedge shaped. In the plateau areas of the HDG substrate, zinc corroded preferentially at the Zn/Steel interface. In the through areas, both the Zn/Steel and Zn/pretreatment interfaces were preferentially attacked.
- The main solid corrosion products were simonkolleite and hydrozincite. In addition, ε-$Zn(OH)_2$ was detected close to the corrosion front on all samples except the phosphated ones.

7. Outlook

Many questions remain open for future studies to answer. One of the most important questions is in regard to the correlation between the laboratory exposures and field exposures, which are currently being conducted. Furthermore, the questions regarding what role the adhesion between the paint system and substrate play in the current exposure regime are unanswered.

There are also many unanswered questions regarding the thin film pretreatments themselves. These questions exist, for instance, in regards to the stability of the pretreatment layers during corrosion. Also, it is unclear whether or not morphology and composition of the pretreatment layer can be linked to the corrosion performance. Questions regarding the environment inside the corrosion blisters during the cyclic exposure conditions, as well as the nature of the corrosion front are still left unanswered.

8. Acknowledgment

I would first like to thank my manager, Mr. Anders Makkonen, for giving me the opportunity to work on this project, as well as for his support over the years.

I would like to thank my supervisors Prof. Lars-Gunnar Johansson, Dr Håkan Mattsson, Annabelle Jaako, and Dr. Dan Persson for sharing their knowledge and expertise in the field of atmospheric corrosion, as well as in the field of automotive pretreatment and corrosion testing.

To Dr. Torbjörn Johansson and Dr. Mohammad Satari for taking the time to discuss microscopy and sample preparation techniques.

A special thanks to Mr. Mats Ström who helped with interesting discussions and ideas.

To all my colleagues at both Chalmers and Volvo for their kindness, especially Mr. Jesper Alm, Mrs. Lisa Lundberg-Lenell, and Mr. Håkan Rodin for always brightening up the day.

To Dr. Johan Nordström for taking the time to discuss my thesis, and for giving me valuable pointers.

Many thanks to Dr. Anders Kvist and Mr. Ola Löfgren for helping with technical issues related to the electron microscopy.

For helping with administrative issues, I would like to thank Mrs. Sandra Gustafson, Mrs. Charlotte Bouveng, and Mrs. Christina Anderson

Last, but not least I would like to thank my wife, Elin Tarka, for being supporting, loving, and patient during my long hours. We are truly flamingos.

Konrad Tarka

November 2015, Gothenburg Sweden

9. References

[1] U.S. Geological Survey, “Mineral commodity summaries 2015,” 2015.

[2] A. I. Taub, P. E. Krajewski, A. A. Luo, and J. N. Owens, “The evolution of technology for materials processing over the last 50 years: the automotive example,” *JOM*, vol. 59, no. 2, pp. 48–57, 2007.

[3] G. Bush, “Developments in the continuous galvanizing of steel,” *JOM*, vol. 41, no. 8, pp. 34–36, 1989.

[4] D. A. Jones, *Principles and prevention of corrosion*, 2nd ed. Harlow: Pearson Education, 2014.

[5] H. S. Wroblowa, “Intermediate products of atmospheric oxygen reduction and the integrity of metal—organic coating interface,” *J. Electroanal. Chem.*, vol. 339, pp. 31–40, 1992.

[6] B. Beverskog and I. Puigdomenech, “Revised pourbaix diagrams for zinc at 25–300 °C,” *Corros. Sci.*, vol. 39, no. 1, pp. 107–114, 1997.

[7] R. Lindström, J.-E. Svensson, and L.-G. Johansson, “The Atmospheric Corrosion of Zinc in the Presence of NaCl - The Influence of Carbon Dioxide and Temperature,” *J. Electrochem. Soc.*, vol. 147, no. 5, pp. 1751–1757, 2000.

[8] R. Lindström, J.-E. Svensson, and L. G. Johansson, “The Influence of Salt Deposits on the Atmospheric Corrosion of Zinc. The Important Role of the Sodium Ion,” *J. Electrochem. Soc.*, vol. 149, no. 2, pp. B57–B64, 2002.

[9] D. L. Hartmann, A. M. G. Klein Tank, M. Rusticucci, L. V Alexander, S. Brönnimann, Y. Charabi, F. J. Dentener, E. J. Dlugokencky, D. R. Easterling, A. Kaplan, B. J. Soden, P. W. Thorne, M. Wild, and P. M. Zhai, “Observations: Atmosphere and Surface,” in *Climate Change 2013: The Physical Science Basis. Contribution of Working Group I to the Fifth Assessment Report of the Intergovernmental Panel on Climate Change*, T. F. Stocker, D. Qin, G.-K. Plattner, M. Tignor, S. K. Allen, J. Boschung, A. Nauels, Y. Xia, V. Bex, and P. M. Midgley, Eds. Cambridge: Cambridge University Press, 2013.

[10] C. Leygraf, “Atmospheric Corrosion,” in *Corrosion Mechanisms in Theory and Practice*, Third., P. Marcus, Ed. CRC Press, 2012, pp. 669–704.

[11] ISO 9223:2012, Corrosion of metals and alloys – Corrosivity of atmospheres – Classification, determination and estimation.

[12] G. L. Song and A. Atrens, “Corrosion Mechanisms of Magnesium Alloys,” *Adv. Eng. Mater.*, vol. 1, no. 1, pp. 11–33, 1999.

[13] Z. Y. Chen, D. Persson, and C. Leygraf, “Initial NaCl-particle induced atmospheric corrosion of zinc-Effect of CO_2 and SO_2,” *Corros. Sci.*, vol. 50, no. 1, pp. 111–123, 2008.

[14] D. Persson and C. Leygraf, “Initial Interaction of Sulfur Dioxide with Water Covered Metal Surfaces: An In,” *J. Electrochem. Soc.*, vol. 142, no. 5, pp. 1459–1468, 1995.

[15] F. Samie, J. Tidblad, V. Kucera, and C. Leygraf, “Atmospheric corrosion effects of HNO_3-Influence of temperature and relative humidity on laboratory-exposed copper,” *Atmos. Environ.*, vol. 41, no. 23, pp. 1374–1382, 2007.

[16] Q. Qu, C. Yan, Y. Wan, and C. Cao, “Effects of NaCl and SO_2 on the initial atmospheric corrosion of zinc,” *Corros. Sci.*, vol. 44, no. 12, pp. 2789–2803, Dec. 2002.

[17] J.-E. Svensson, “The influence of different air pollutants on the atmospheric corrosion of zinc,” Ph.D dissertation, Chalmers Institute of Technology, 1995.

[18] L. Veleva and R. D. Kane, “Atmospheric Corrosion, Corrosion: Fundamentals, Testing, and Protection, Vol 13A,” in *ASM Handbook*, 2003, pp. 196–209.

[19] I. S. Cole, W. D. Ganther, J. D. Sinclair, D. Lau, and D. A. Paterson, “A Study of the Wetting of Metal Surfaces in Order to Understand the Processes Controlling Atmospheric Corrosion,” *J. Electrochem. Soc.*, vol. 151, no. 12, pp. B627–B635, 2004.

[20] A. K. Neufeld, I. S. Cole, A. Bond, and S. A. Furman, “The initiation mechanism of corrosion of zinc by sodium chloride particle deposition,” *Corros. Sci.*, vol. 44, no. 3, pp. 555–572, 2002.

[21] J.-E. Svensson and L.-G. Johansson, “A laboratory study of the initial stages of the atmospheric corrosion of zinc in the presence of NaCl; inluence of SO_2 and NO_2,” *Corros. Sci.*, vol. 34, no. 5, pp. 721–740, 1993.

[22] F. Zhu, D. Persson, D. Thierry, and C. Taxen, “Formation of Corrosion Products on Open and Confined Zinc Surfaces Exposed to Periodic Wet/Dry Conditions,” *Corrosion*, vol. 56, no. 12, pp. 1256–1265, 2000.

[23] J.-M. Mataigne, V. Vaché, and M. Repoux, “Surface chemistry and reactivity of skin-passed hot dip galvanized coating,” *La Rev. Métallurgie*, vol. 106, no. 1, pp. 41–47, Jan. 2009.

[24] A. V. Gorbunov, V. K. Belov, and D. O. Begletsov, “Texturing of rollers for the production of auto-industry sheet,” *Steel Transl.*, vol. 39, no. 8, pp. 696–699, 2009.

[25] D. K. Aspinwall, M. L. H. Wise, K. J. Stout, T. H. A. Goh, F. L. Zhao, and M. F. El-Menshawy, “Electrical discharge texturing,” *Int. J. Mach. Tools Manuf.*, vol. 32, no. 1–2, pp. 183–193, 1992.

[26] G. Davies, “Materials for Automobile Bodies,” *Mater. Automob. Bodies*, pp. 189–219, 2003.

[27] M. Sporrong, “Personal communication.” Surface Tretment Center at Volvo Car Corporation, 2015.

[28] T. S. N. S. Narayanan, “Surface pretreatment by phosphate conversion coatings - a review,” *Rev. Adv. Mater. Sci.*, no. 9, pp. 130–177, 2005.

[29] A. Sabata, “Study of the corrosion mechanisms in modern painted precoated automotive sheet steels,” Ph.D dissertation, Colorado School of Mines Golden, Colorado, 1989.

[30] J. Fonselius, “Kurs i kemisk förbehandling.” 2004.

[31] P.-E. Tegehall and N.-G. Vannerberg, “Nucleation and formation of zinc phosphate conversion coating on cold-rolled steel,” *Corros. Sci.*, vol. 32, no. 5–6, pp. 635–652, 1991.

[32] W. Machu, *Die Phosphatierung*. Weinnharin: Verlag-Chemie, 1950.

[33] K. Ogle, “The alkaline stability of phosphate coatings I : ICP atomic emission spectroelectrochemistry,” *Corros. Sci.*, vol. 46, pp. 979–995, 2004.

[34] P.-E. Tegehall, “The mechanism of chemical activation with titanium phosphate colloids in the formation of zinc phosphate conversion coatings,” *Colloids and Surfaces*, vol. 49, pp. 373–383, 1990.

[35] K. Ogle and M. Wolpers, “Phosphate Conversion Coatings,” in *Corrosion: Fundamentals, Testing and Protection, Vol 13A, ASM Handbook*, 2003, pp. 712–719.

[36] B. Rösner, “Personal communication.” .

[37] S. Adhikari, K. A. Unocic, Y. Zhai, G. S. Frankel, J. Zimmerman, and W. Fristad, “Hexafluorozirconic acid based surface pretreatments : Characterization and performance assessment,” *Electrochim. Acta*, vol. 56, no. 4, pp. 1912–1924, 2011.

[38] O. Lunder, J. Walmsley, and C. J. Simensen, “Formation of a Ti-Zr based conversion coating on AA6060 aluminium,” *SIP seminar*. Oslo, 2002.

[39] O. Lunder, F. Lapique, B. Johnsen, and K. Nisancioglu, “Effect of pre-treatment on the durability of epoxy-bonded AA6060 aluminium joints,” *Int. J. Adhes. Adhes.*, vol. 24, pp. 107–117, 2004.

[40] O. Lunder, C. Simensen, Y. Yu, and K. Nisancioglu, “Formation and characterisation of Ti – Zr based conversion layers on AA6060 aluminium,” *Surf. Coatings Technol.*, vol. 184, pp. 278–290, 2004.

[41] F. O. George, P. Skeldon, and G. E. Thompson, “Formation of zirconium-based conversion coatings on aluminium and Al–Cu alloys,” *Corros. Sci.*, vol. 65, pp. 231–237, Dec. 2012.

[42] F. Andreatta, A. Turco, I. De Graeve, H. Terryn, J. H. W. De Wit, and L. Fedrizzi, “SKPFM and SEM study of the deposition mechanism of Zr / Ti based pre-treatment on AA6016 aluminum alloy,” *Technology*, vol. 201, pp. 7668–7685, 2007.

[43] T. Lostak, S. Krebs, A. Maljusch, T. Gothe, M. Giza, M. Kimpel, J. Flock, and S. Schulz, “Formation and characterization of Fe^{3+}-/Cu^{2+}-modified zirconium oxide conversion layers on zinc alloy coated steel sheets,” *Electrochim. Acta*, vol. 112, pp. 14–23, Dec. 2013.

[44] B. Schneider, A. Drews, M. Jagner, S. J. Simko, and J. L. Tardiff, “Characterization of Zirconium Oxide-Based Pretreatment Coatings Part 2 – Challenges in Coating Aluminum Body Panels,” *Innovation*, 2009.

[45] W. J. van Ooij, D. Zhu, M. Stacy, A. Seth, T. Mugada, J. Gandhi, and P. Puomi, “Corrosion Protection Properties of Organofunctional Silanes — An Overview,” *Tsinghua Sci. Technol.*, vol. 10, no. 6, pp. 639–664, 2005.

[46] O. I and W. M., “Zinc chlorohydroxosulfates: newly- discovered corrosion products on zinc. Structure determination of $NaZn_4Cl(OH)_6SO_4 \bullet 6H_20$ and X-ray study of $Zn_4Cl_2(OH)_4SO_4 \bullet 5H_20$,” *Corros. Sci.*, vol. 34, no. 8, pp. 1231–1242, 1993.

[47] V. Palanivel and W. J. Van Ooij, “Modified silane coatings as an alternative to chromates for corrosion protection of aluminum alloys,” 3rd ed., K. L. Mittal, Ed. CRC Press, 2004, pp. 135–159.

[48] V. Palanivel, D. Zhu, and W. J. Van Ooij, “Nanoparticle-filled silane films as chromate replacements for aluminum alloys,” *Prog. Org. Coatings*, vol. 47, pp. 384–392, 2003.

[49] M. F. Montemor, A. Rosqvist, H. Fagerholm, and M. G. S. Ferreira, “The early corrosion behaviour of hot dip galvanised steel pre-treated with bis-1, 2-(triethoxysilyl)ethane,” *Prog. Org. Coatings*, vol. 51, pp. 188–194, 2004.

[50] D. Persson, “Personal communication.” 2015.

[51] T. Bruhn, “Personal communication,” 2015.

[52] A. Amirudin and D. Thierry, “Corrosion mechanisms of phosphated zinc layers on steel as substrates for automotive coatings,” *Prog. Org. Coatings*, vol. 28, pp. 59–76, May 1996.

[53] W. Fürbeth and M. Stratmann, “Delamination of polymeric coatings from electrogalvanized steel - a mechanistic approach. Part 2: Delamination from a defect down to steel,” *Corros. Sci.*, vol. 43, pp. 229–241, 2001.

[54] W. Fürbeth and M. Stratmann, “The delamination of polymeric coatings from electrogalvanised steel-a mechanistic approach.-Part 1: delamination from a defect with intact zinc layer,” *Corros. Sci.*, vol. 43, pp. 207–227, 2001.

[55] W. Fürbeth and M. Stratmann, “The delamination of polymeric coatings from electrogalvanised steel – a mechanistic approach. Part 3: delamination kinetics and influence of CO_2,” *Corros. Sci.*, vol. 43, no. 2, pp. 243–254, 2001.

[56] R. D. Granata, “NACE Annual Corrosion Conference,” 1991, Paper No 382.

[57] A. Leng, H. Streckel, and M. Stratmann, “The delamination of polymeric coatings from steel. Part 2: First stage of delamination, effect of type and concentration of cations on delamination, chemical analysis of the interface,” *Corros. Sci.*, vol. 41, no. 3, pp. 579–597, 1999.

[58] C. R. Shastry and H. E. Townsend, “Mechanisms of Cosmetic Corrosion in Painted Zinc and Zinc-Alloy-Coated Sheet Steels,” *Corrosion*, vol. 45, 1989.

[59] N. S. Sangaj and V. C. Malshe, “Permeability of polymers in protective organic coatings,” *Prog. Org. Coatings*, vol. 50, no. 1, pp. 28–39, 2004.

[60] R. D. Armstrong and B. W. Johnson, “An investigation into the cathodic delamination of unpigmented chlorinated rubber films,” *Corros. Sci.*, vol. 32, no. 3, pp. 303–312, 1991.

[61] W. J. Van Ooij, A. Sabata, D. Loison, T. Jossic, and J.-C. Charbonnier, “Paint delamination from electrocoated automotive steels during atmospheric corrosion. Part I. Hot-dip galvanized and electrogalvanized steel,” *J. Adhes. Sci. Technol.*, vol. 3, no. 1, pp. 1–27, 1989.

[62] D. D. Davidson and W. A. Schumarcher, “Paper No. 912284,” in *Proc. 5th Automotive Corrosion Prevention Conference.*, 1991, p. 205.

[63] M. Ström, G. Ström, W. J. van Ooij, A. Sabata, and B. A. Knueppel, in *Proc. 2nd Int. Conf. on Zn and Zn Alloy-Coated Steel Sheet, GALVATECH’92*, 1992, p. 521.

[64] M. Ström, in *Proc. Eur. Conf. Future Practice of Environmental Engineering in product Development*, 1992.

[65] W. J. van Ooij, A. Sabata, and G. Ström, in *Corrosion Resistant Automotive Sheet Steels, World Materials Congr.*, 1988, p. 75.

[66] K. Ogle, S. Morel, and N. Meddahi, “An electrochemical study of the delamination of polymer coatings on galvanized steel,” *Corros. Sci.*, vol. 47, pp. 2034–2052, 2005.

[67] A. Nazarov, M. Olivier, and D. Thierry, “SKP and FT-IR microscopy study of the paint

corrosion de-adhesion from the surface of galvanized steel," *Prog. Org. Coatings*, vol. 5, 2011.

[68] R. Reichelt, "Scanning Electron Microscopy," in *Science of Microscopy*, New York: Springer, 2007, pp. 133–268.

[69] D. . Williams and B. . Carter, *Transmition electron microscopy*. New York: Springer, 1996.

[70] M. . Woolfson, *An introduction to X-Ray Crystallography*. Cambridge: Cambridge University Press, 1970.

[71] G. Jönsson and E. Nilsson, *Tillämpad atomfysik*. Lund: Teach Support, 2005.

[72] "VCS - 1021,29 Scribing of coated test object and evaluation of propagation of corrosion from scribed line." Volvo Car Corporation, 2007.

[73] "VCS 1027,1449 - Accelerated corrosion test – ACT II." Volvo Car Corporation, 2011.

[74] O. K. Srivastava and E. A. Secco, "Studies on metal hydroxy compounds . II . Infrared spectra of zinc derivatives e- $Zn(OH)_2$, b-ZnOHCl, ZnOHF, $Zn_5(OH)_8Cl_2$ and $Zn_5(OH)_8Cl_2 \cdot H_2O$," *Can. J. Chem.*, vol. 45, pp. 585–588, 1967.

[75] A. Stoch, C. Paluszkiewicz, and E. Długoń, "An effect of methylaminoethoxysilane on zinc phosphate rehydration," *J. Mol. Struct.*, vol. 511–512, pp. 295–299, Nov. 1999.